UNIVERSITY OF CINCINNATI

Date: September 7, 2004

I, Divakar Rajamohan **,**

hereby submit this work as part of the requirements for the degree of:

Master of Science

in:

Mechanical Engineering

It is entitled:

Developing Pulsatile Flow in a Deployed Coronary Stent

This work and its defense approved by:

Chair: Dr. Rupak K. Banerjee

Dr. Milind A. Jog

Dr. Edward S. Grood

Developing Pulsatile Flow in a Deployed Coronary Stent

A thesis submitted to the

Division of Research and Advanced Studies
of the University of Cincinnati

in partial fulfillment of the
requirements for the degree of

MASTER OF SCIENCE

in the Department of Mechanical, Industrial and Nuclear Engineering
of the College of Engineering

2004

by

Divakar Rajamohan

Bachelor of Engineering, Regional Engineering College, Trichy, India 2001

Committee Chair: Dr. Rupak K. Banerjee

ABSTRACT

A major consequence of stent implantation is restenosis that occurs due to neointimal formation. Recent evidence suggests that there are several factors such as geometry and size of vessel, and stent design that alters hemodynamic parameters, including local wall shear stress distributions, which influence the progression of restenosis. The present three-dimensional analysis of developing pulsatile flow in a deployed coronary stent quantifies hemodynamic parameters and illustrates the changes in local wall shear stress distributions and their impact on restenosis. The present model mimics the worst possible scenario where the stent is placed at the entrance region of a branched coronary artery. The present results indicate that the immediate downstream of strut intersections are areas highly susceptible to restenosis whereas a high shear stress at the strut intersection may cause platelet activation and free emboli formation.

ACKNOWLEDGEMENT

First and foremost, I am grateful to my advisor Dr. Rupak Banerjee who has provided me continuous support and guidance throughout the course of my work. His ideas and discussions have been critical to the successful completion of this research work. I would like to thank Dr. Milind Jog, Dr. Christy Holland, Dr. Ed Grood and Dr. Randall Wolf of the University of Cincinnati for their assistance in reviewing the results and being the members of my thesis defense committee.

I would like to thank the Department of Mechanical, Industrial and Nuclear Engineering at the University of Cincinnati for providing this opportunity to study. I would like to thank my colleague, Ashraf Ibrahim who has helped me at various times. I am also thankful to all the members of Bio-Fluids, Heat & Mass Laboratory with whom I had the opportunity to interact and discuss my work. I would like to thank my friends for their moral support and assistance during this course work. Sincere thanks to my parents and sister for their constant motivation, affection and support while I have been away from home.

TABLE OF CONTENTS

LIST OF FIGURES

LIST OF FIGURES (Continued)

NOMENCLATURE

d	vessel diameter, cm
p	static pressure, mm Hg
Δp	pressure drop, ($p_{out} - p_{in}$), mm Hg
$\tilde{Q}$	mean flow rate, ml/min
r	radial distance from the vessel axis, cm
$\tilde{\mathrm{Re}}$	mean-flow Reynolds number, ($4\tilde{Q}/\pi\nu d$)
t	time, s
u	axial velocity, cm/s
$\vec{v}$	velocity vector, cm/s
Z	axial distance, cm
α	frequency parameter, $(d/2)(\omega/\nu)^{0.5}$
$\dot{\gamma}$	shear rate, s^{-1}
$\dot{\gamma}_{ij}$	rate of strain tensor, s^{-1}
μ	molecular viscosity, poise
η	blood viscosity, poise
ν	kinematic viscosity, η/ρ, cm^2/s
ρ	density, g/cm^3
τ	wall shear stress [WSS], dyn/cm^2
$\bar{\bar{\tau}}$	stress tensor, dyn/cm^2
T	period of cardiac cycle, s
ω	circular frequency, $2\pi/T$, s^{-1}

Subscript

in	inlet of artery
out	outlet of artery
w	wall condition

Superscript

~	time-average (mean over cardiac cycle)

CHAPTER 1: INTRODUCTION

Interventional techniques like balloon angioplasty with and without stent placement are used to treat arterial stenosis. American Heart Association statistics [1] show serious complications in 1-2% of cases following Percutaneous Transluminal Coronary Angioplasty (PTCA). In contrast, after 6 months following procedure, 30-40% of patients develop restenosis. Thus there is statistical significance between contrasting scenarios of mortality and restenosis. Stent implantation improves the arterial blood flow by redistributing the plaque. A major consequence of stent implantation is restenosis which occurs due to neointimal formation around the deployed stent. The main benefit of stenting compared with conventional PTCA consists of reduction of restenosis. Though stents are used to increase the arterial lumen diameter and restore blood flow, restenosis could not be completely eliminated and remains a persistent problem in a substantial number of patients treated with this modality (Erbel et al. [2], Fischman et al. [3] and van Beusekom et al. [4]).

There are several factors affecting restenosis like geometry and size of vessel, and stent design that impacts areas of flow recirculation and flow separation and wall shear stress [5, 6, 8, 16 and 17]. Kastrati et al. [5] have performed a detailed analysis of the relation between clinical, lesion, and procedural factors and restenosis after intracoronary stenting of 8 different stent designs in a series of patients. In their investigation, among these factors vessel size was observed to be the most predominant factor affecting restenosis and stent design was the second strongest risk factor, playing an important role in the hyperplastic response of the vessel wall. Also they found a higher risk to be associated with smaller vessel size, complex lesions, and longer lesions.

Kastrati et al. [6] have studied the effect of strut thickness of coronary stents on restenosis where thin strut stent of strut thickness 50 μm and thick strut stent of thickness 140 μm were implanted in a group of patients. The incidence of angiographic restenosis was 15% in the thin-strut group and 25.8% in the thick-strut group. The reintervention rate was 8.6% among thin-strut patients and 13.8% among thick-strut patients. A significant reduction of 42% angiographic restenosis and 38% clinical restenosis was observed in stents constructed with thin metal struts compared to stents with thick metal struts. The early mortality rate was 1.5% among thin-strut patients and 2.5% among thick-strut patients. Vrints et al. [7] have performed a comparative study of coil and tubular stents and analyzed the effects of stenting on coronary flow velocity reserve. They have observed the incidence and severity of restenosis to vary with stent type. These data suggest that stent geometry and its subsequent effects on localized fluid dynamics may be risk factors for restenosis.

Geometric design factors for a deployed stent affecting restenosis are areas of flow recirculation and flow separation [6 – 10]. Berry et al. [8] have shown that stent geometry has a significant effect on local hemodynamics by performing a flow analysis in a simulated coronary artery with a deployed metallic stent. In their study, dye injection flow visualization and computational fluid dynamics were carried out. It was seen that more dye got accumulated between the stent wires when the wire spacing was the smallest (3 wire diameters) and the stagnation zones were continuous from one wire to the next. Whereas, in large wire spacing two separate stagnation zones were observed and flow reattachment occurred between the wires. They concluded that the optimum wire spacing is 6 wire diameters. Moore and Berry [9] and Frank et al. [10] have shown the dependence of flow recirculation and flow reattachment on strut spacing. They observed minimum platelet deposition and continual flow stagnation at low strut

spacing, maximum platelet deposition and partial flow reattachment at intermediate strut spacing, and high platelet deposition and complete flow reattachment at higher strut spacing.

Barakat and Cheng [11], and Barakat and Schachter [12] have analyzed the flow recirculation by carrying out a two dimensional steady flow simulation of an axisymmetric stented geometry under steady and pulsatile flow conditions. They showed that the zones of flow separation and flow recirculation have low wall shear stress values and the flow recirculation length increases with flow Reynolds number and stent wire thickness. Caro et al. [13] and Nerem et al. [14] have shown that recirculation zones of low shear stresses are susceptible to the deposition of macromolecules and other lipid derivatives.

Another important factor affecting restenosis is the wall shear stress (WSS) gradient [15 – 17]. Henry [15] has carried out simulations of flow through model stented arteries which showed flow separation over a short distance on either side of the strut. He concluded that the occurrence of flow separation led to large WSS gradients in the immediate vicinity of the flow separation and reattachment points, and this might have an impact on the rate of endothelial repair following injury induced by stent placement.

Wentzel et al. [16] have investigated the relationship between local variations in shear stress and neointimal thickness after stent placement and have stated that neointimal thickness is inversely related to shear stress. They reported that at 6 month follow up after coronary wallstent implantation, low shear stress regions showed maximal neointimal formation and high shear stress showed minimal neointimal formation. Wentzel et al. [17] have evaluated the regional changes in three dimensional geometry and shear stress distribution after coronary wallstent placement in curved coronary arteries of swine. After stent implantation, the curvature of artery was observed to increase by 121% at the entrance of the stent which increased the

maximal shear stress by 74% and by 113% for low and high flow conditions, respectively. At the exit of the stent, the curvature of artery was observed to increase by 100% which increased the maximal shear stress by 30% for low flow conditions and decreased the minimal shear stress by 54% for high flow conditions. These computational fluid dynamics modeling studies have used vascular geometries that approximate the stented region of the vessel wall and focused primarily on the most prominent areas of restenosis. This has led to the conclusion that shear stress plays an essential role in plaque and thrombus formation and is sensitive to variations in regional vessel geometry.

Berry et al. [18] have studied the compliance mismatch existing between stent ends and the artery wall which affects the local WSS distribution. They have performed *in vitro* and *in vivo* analysis comparing a compliance matching stent and Palmaz stent in a swine model where the compliance matching stent showed reduced circumferential stress in the arterial wall and minimal neointimal accumulation. Fontaine et al. [19] have analyzed the difference between flexible and rigid stent designs and stated that stent design play a major role in the incidence and severity of restenosis.

Rogers et al. [20] and Edelman and Rogers [21] have correlated the local hemodynamics with the formation of plaque layers, particularly at the site of low wall shear stress. Their studies showed a vital role for tissue damage in neointimal hyperplasia due to the stent design. However, fluid flow is also responsible for the neointimal hyperplasia that occurs during in-stent restenosis. Ku et al. [22] and Sabbah et al. [23] performed hemodynamic analysis in human carotid bifurcation and left anterior descending coronary artery, respectively. They have related atherosclerosis to arterial wall shear stress and provided a positive correlation between plaque location and low oscillating shear stress. Study of fluid wall shear stress measurements in a

model of the human abdominal aorta support the well-established observation that areas of maximal intimal thickening correlate with regions of low (less than 4 dyn/cm^2) and oscillatory wall shear stress (Moore et al. [24]). These studies have also concluded that regions of high shear stress (greater than 12 dyn/cm^2) protect against intimal hyperplasia.

Coronary arteries receive blood flow directly from the aorta. The aortic flow is of developing nature in the entrance sections of coronary arteries at systole. Suo et al. [25] have studied the coronary entrance flow patterns that are affected strongly by flow in the aorta root. He observed that the developing flow parameters, such as velocity profiles and WSS distributions deviated significantly from flows that were fully developed.

LaDisa et al. [26] have studied the localized alterations in WSS produced by coronary stent implantation by performing a three dimensional computational fluid dynamics analysis with the assumptions of blood to be a Newtonian fluid and flow to be steady. They observed that the regions of low WSS and the stagnation zones occurred around the stent struts where the minimum WSS decreased by 77% in stented vessel compared to unstented vessel.

Bluestein et al. [27] have performed a study on the formation of free emboli in the wake of bi-leaflet mechanical valves and quantified the effect of a misaligned valve on platelet activation and compared to that of an aligned valve. They showed that non-physiological flow patterns past the valve that cause elevated shear stress values of 20 dyn/cm^2 and shed vortices in the wake of valve's leaflets during the deceleration phase lead to the formation of free emboli and platelet aggregation.

Although there have been several studies of coronary flow and physiological consequences of restenosis after stent placement, the effect of stent implantation on local WSS distribution as well as other fluid dynamic parameters and its influence on restenosis are not well

quantified. The present work focuses on a detailed study of WSS distribution and other hemodynamic parameters like recirculation length and height for a Palmaz stent that is deployed under the worst scenario: at the origin of a branched coronary artery causing the flow to be developing in nature. This study improves upon previously published literatures as a three dimensional analysis has been conducted to quantify the stent induced changes on the flow patterns for a pulsatile flow from basal to hyperemic conditions with the Carreau model, chosen for shear-rate-dependent non-Newtonian viscosity of blood. The flow field was complex in the mean flow Reynolds number range, $\tilde{\mathrm{Re}}$ = 108 – 430 and frequency parameter, α = 2.32.

CHAPTER 2: METHODOLOGY

2.1 Geometry

A pulsatile flow analysis is performed for a freshly deployed Palmaz stent in a human coronary artery having a three dimensional geometry with an axial length of 10 mm and diameter of 3 mm as shown in figure 1. The struts of the stent are circular in shape with diameter of 0.4 mm and the stut spacing i.e. the axial distance between two consecutive struts of 2.5 mm. Following the deployment of the stent, it is assumed that half of the stent is exposed to the blood flow whereas the other half of the stent is embedded in the arterial wall.

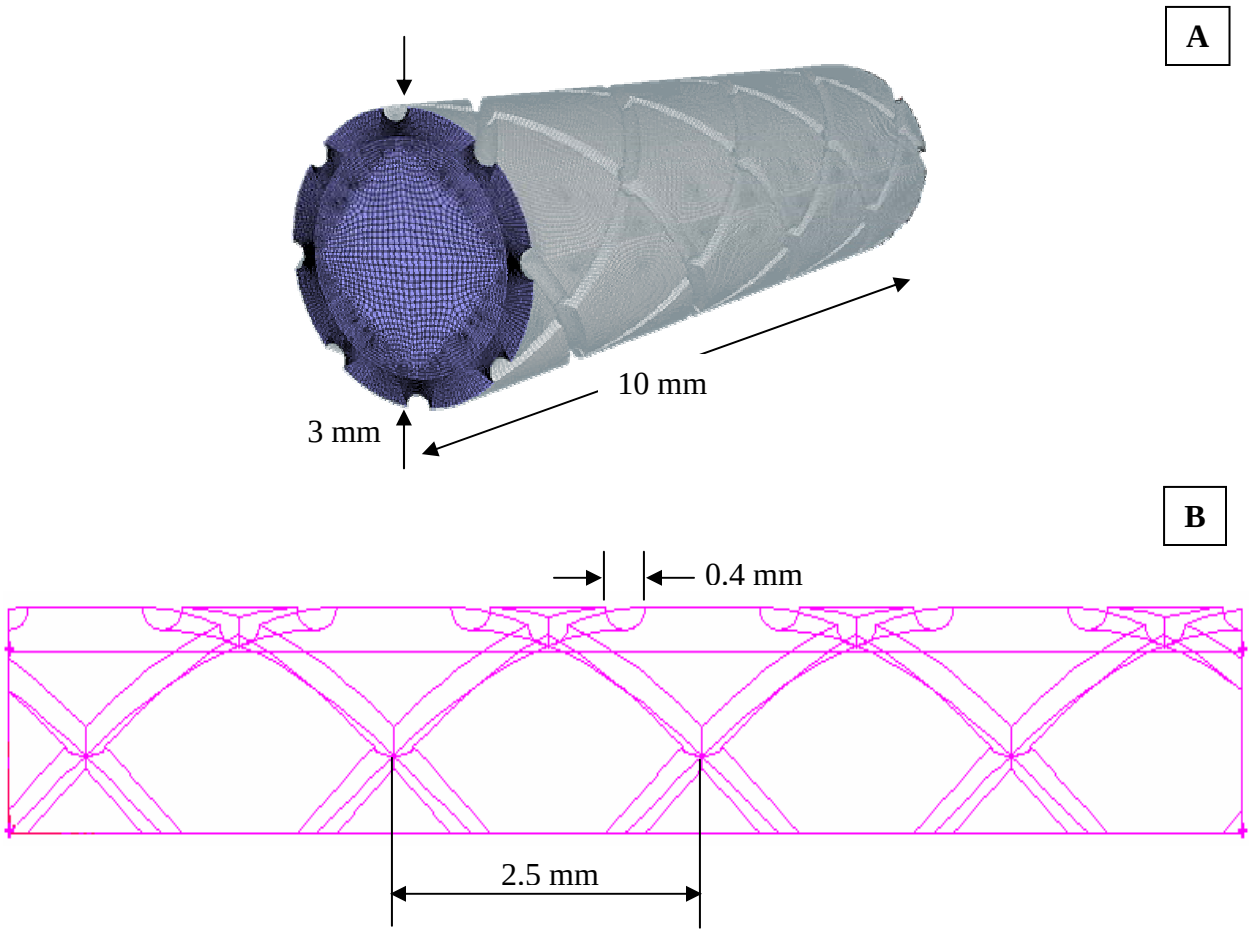

Figure 1. Mesh Plot of Coronary Artery with Deployed Palmaz Stent (A) and Geometry of the Stent Struts (B)

2.2 Flow Pulse

The coronary flow waveform (Fig. 2) used in the flow simulations was obtained from *in vitro* calibration (Cho et al. [28]) and smoothing the fluctuating Doppler signal. The spatially averaged velocity $(\bar{u}(t))$ across the flow needed for flow simulations is similar to that from Doppler catheter measurements in the left anterior descending (LAD) and left circumflex (LCX) coronary arteries of patients undergoing percutaneous transluminal coronary angioplasty (Sibley at al. [29] and Banerjee et al. [30]). The systole and diastole periods are shown in figure 2. The ratio of peak systolic to peak diastolic velocity is 0.4 and the ratio of mean to peak velocity is 0.537.

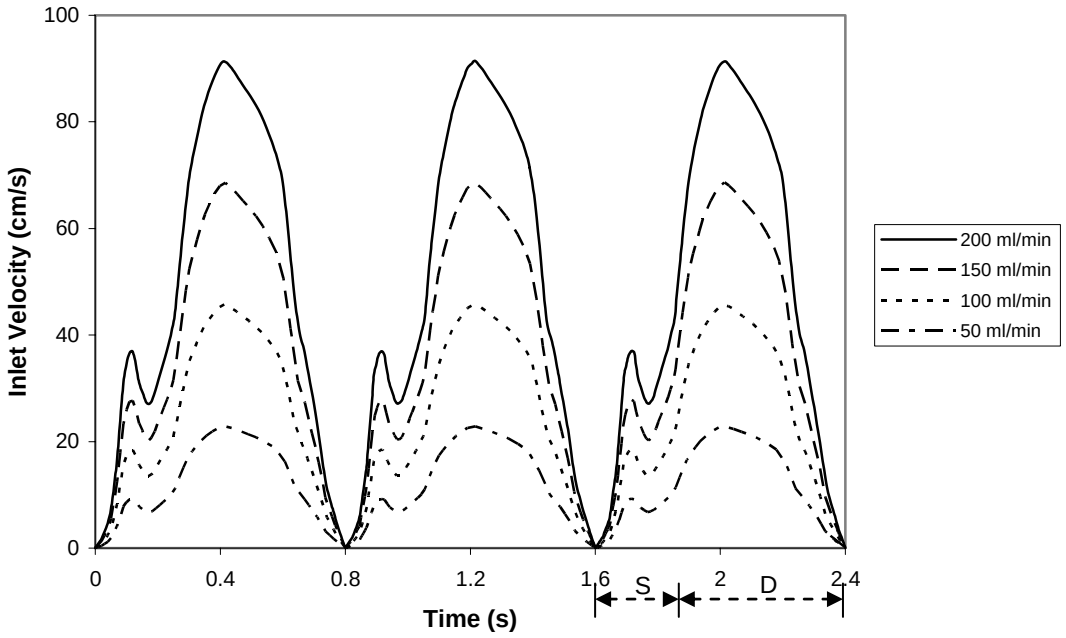

Figure 2. Pulse Cycles for Basal to Hyperemic Flows; S – systole, D – diastole

2.3 Governing Equations

The flow simulations were carried out by numerically solving the following continuity and Navier-Stokes momentum equations for pulsatile blood flow (Banerjee et al. [31]) using a finite volume method.

Mass conservation equation:

$$\rho\nabla.(\vec{v}) = 0 \tag{1}$$

where ρ is the density of blood and $\vec{v}$ is the velocity vector.

Momentum conservation equation:

$$\rho\frac{\partial}{\partial t}(\vec{v}) + \rho\nabla.(\vec{v}\vec{v}) = -\nabla p + \nabla.(\bar{\bar{\tau}}) \tag{2}$$

where p is the static pressure and $\bar{\bar{\tau}}$ is the stress tensor. The stress tensor $\bar{\bar{\tau}}$ is given by,

$$\bar{\bar{\tau}} = \mu\left[\left(\nabla.\vec{v} + \nabla.\vec{v}^{T}\right)\right] \tag{3}$$

where μ is the molecular viscosity.

As blood is a non-Newtonian fluid, for the present study the Carreau model is used for shear-rate-dependent non-Newtonian viscosity of blood with local shear rate calculated from the velocity gradient through the second invariant of the rate of strain tensor (Cho and Kensey [32]). The corresponding equations for local shear rate $\dot{\gamma}$ and blood viscosity η are given by,

$$\dot{\gamma} = \sqrt{\frac{1}{2}\left[\sum_{i}\sum_{j}\dot{\gamma}_{ij}\dot{\gamma}_{ji}\right]} \tag{4}$$

where $\dot{\gamma}_{ij}$ is the rate of strain tensor and i,j = 1,2,3 for three dimensional flows.

$$\eta = \eta_{\infty} + (\eta_0 - \eta_{\infty})\left[1 + (\lambda\dot{\gamma})^2\right]^{(n-1)/2} \tag{5}$$

where, time constant λ = 3.313 s, power law index n = 0.3568, zero shear viscosity η_0 = 0.56 poise and infinite shear viscosity η_∞ = 0.0345 poise. The model constants were obtained by curve-fitting blood viscosity data in the literature. The density of blood is taken to be 1.05 g/cm^3. From these relations, the local shear stress $\tau = \eta\dot{\gamma}$ is calculated. In our reported value of $\tilde{\mathrm{Re}}$ and α, a kinematic viscosity of ν = 0.0329 cm^2/s was used (the asymptote in the Carreau model).

2.4 Oscillatory Shear Index (OSI) and Modified Oscillatory Shear Index (MOSI)

OSI is the ratio of absolute value of time averaged WSS to time averaged absolute value of WSS given by,

$$\mathrm{OSI} = \frac{\left|\int_0^t \tau_w dt\right|}{\int_0^t |\tau_w| dt} \tag{6}$$

The arterial wall has both positive and negative shear stress during the pulse cycle. Since OSI gives a positive value irrespective of the sign of the WSS, it is modified by removing the modulus in equation (6) in order to distinguish the regions of positive and negative WSS.

$$\mathrm{MOSI} = \frac{\int_0^t \tau_w dt}{\int_0^t |\tau_w| dt} \tag{7}$$

MOSI value of 1 implies a positive WSS during the entire cardiac cycle; 0 implies that both positive and negative shear stress being equal in magnitude; and -1 implies a negative shear stress during the entire cardiac cycle. Thus MOSI helps in identifying the zones of recirculation which have negative WSS values.

2.5 Boundary Conditions

To model the worst flow scenario at the entrance region of the artery, a time-varying pulse (Fig. 2A) with a uniform spatial variation of velocity boundary condition is imposed at inlet with a user-defined subroutine programmed in C. The uniform velocity boundary condition simulated the worst scenario, providing maximum shear stress at the wall. Thus, the present model mimics the stent being deployed at the origin of a branched coronary artery. No-slip boundary condition is specified on the wall which makes all flow velocity components equal to zero. Considering the diseased condition of the coronary artery, the wall is specified to be rigid. At the outlet, stress free condition with zero gauge pressure boundary condition is applied.

2.6 Finite Volume Method

The finite volume mesh was generated in Gambit 2.1.0 using Cooper scheme with ~650,000 cells of hexahedral elements. In order to mesh the deployed stent, the flow domain was sub-divided into two independent regions with non-conformal interfaces between them. The two independent regions are the core lumen zone and the annular region containing the stent cross-links. The two regions were merged at the common interface through advanced mesh interpolation scheme. The volume mesh i.e. the annular region and the interface between the two regions are shown in figure 3.

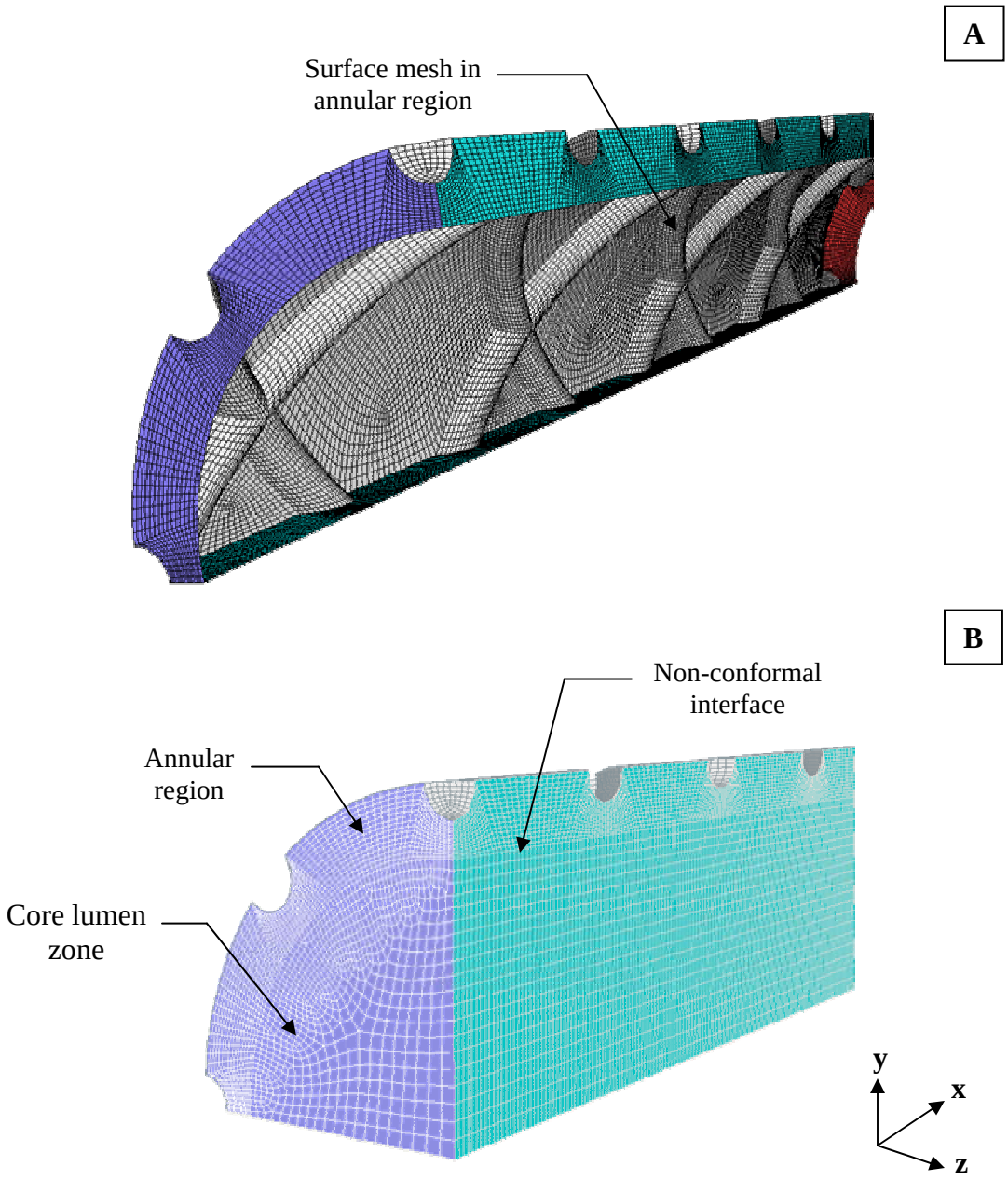

Figure 3. Mesh Details: Volume Mesh (A) and Non-conformal Interface (B)

Equations 1-5 were solved using finite volume method [33]. Three dimensional double precision, segregated and laminar solver was used to solve the equations governing with fluid flow. For the segregated solver, continuity and momentum equations are decoupled from one another and are solved sequentially. Second-order time implicit scheme was employed to discretize the governing equations. Under-Relaxation factors of 0.3 for pressure, 1 for density, and 0.7 for momentum were used. Second order discretization was followed for pressure with simple algorithm chosen for pressure-velocity coupling. A second order upwind scheme was adapted for discretization of momentum. Convergence criterion for continuity and velocity residuals was kept at 10^{-4} an order of magnitude lower than a recommended value. Adaptive time stepping methodology was used for the iterations. Truncation error tolerance of 1e-4, minimum time step size of 1e-4, minimum step change factor of 0.5, maximum step change factor of 1.1 were used. Depending upon the velocity pulse shape, the time steps varied between 10^{-3}s and10^{-4}s.

Mesh independency was checked by increasing the number of elements by 20% over the previous mesh and both the results were compared. The mesh with increased number of elements showed less than 1% difference in velocity and WSS values. Computations were conducted on a Red Hat Linux (Version 7.3) workstation with dual Intel (Xeon IV) 2.4 GHz processors with 1.0 GB RAM and 80 GB hard disk. Simulations were run for four different time averaged (mean) flow rates, $\tilde{Q}$ = 50, 100, 150 and 200 ml/min (basal to hyperemic flow rates). Typical computational run time for a single simulation to complete was 5 days.

The numerical computation was conducted for 3 consecutive pulse cycles with a pulse time period (T) of 0.8 s. The results are reported for the 3rd cycle (1.6 s to 2.4 s). The velocity profiles are calculated at specific time points: 1.86 s, the early acceleration phase

($u_{in} = 0.5\ u_{in_{max}}$); 2.00 s, the peak flow ($u_{in} = u_{in_{max}}$); 2.16 s, the early deceleration phase of the cycle ($u_{in} = 0.75\ u_{in_{max}}$) and 2.30 s, the late deceleration phase of the cycle ($u_{in} = 0.25\ u_{in_{max}}$).

2.7 Validation

WSS data of the present study (coronary stent: d = 0.3 cm, u_{in} = 22.8 cm/s, $\tilde{\mathrm{Re}}$ = 208) is validated with the recent study by LaDisa et al. [26] (coronary stent: d = 0.274 cm, u_{in} = 22.5 cm/s, $\tilde{\mathrm{Re}}$ = 177). Figure 4 shows the comparison of WSS at the four strut intersections of the stent. Due to the developing nature of the flow at the entrance region of the artery and deployed stent, the WSS at strut intersection 1 is 108 dyn/cm^2, which is about twice that of the developed flow (LaDisa et al. [26]). As the flow develops, the WSS value decreases rapidly and the percentage variation in the stress values between the present study and LaDisa et al. [26] work is 12% at strut intersection 2, 2.2% at strut intersection 3, and 0.1% at strut intersection 4. Thus, this study validates the recently published work by LaDisa et al. [26] within 0.1% for the developed flow. This shows the accuracy of the present results. It may be noted that the present study of developing pulsatile flow has not been reported in the past. The additional validation of pressure data of the present study is shown in figure 25B.

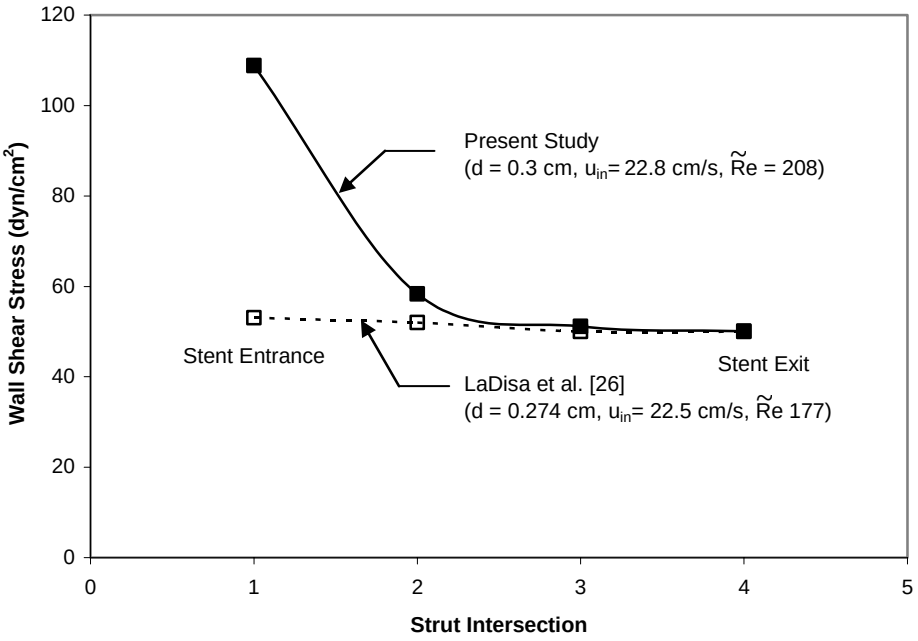

Figure 4. Validation of Wall Shear Stress

CHAPTER 3: RESULTS

To study the effect of stent implantation on blood flow, velocity profiles and WSS are plotted at various points inside the stented artery. Figure 5 shows a pictorial representation of the locations of strut intersections (strut cross-links), midpoints (midpoint of two adjacent strut intersections) and vertices (immediate upstream and downstream of strut intersections) where the velocity profiles and WSS are plotted.

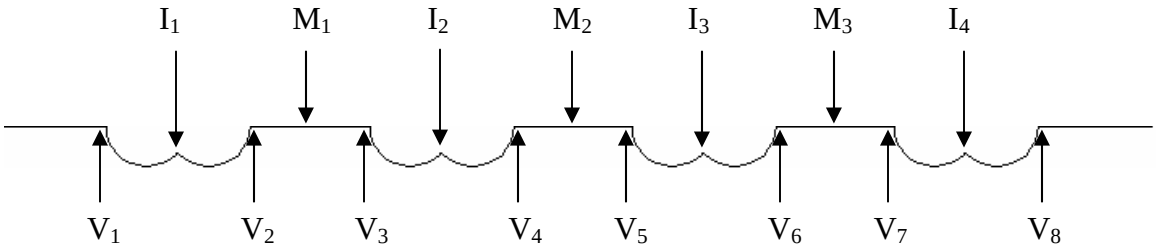

Figure 5. Pictorial Representation of the Locations of Strut Intersections (I), Midpoints (M) and Vertices (V)

Zones of recirculation and flow stagnation are estimated from the WSS plots and the effect of flow rate on recirculation is observed by plotting the recirculation length and height for basal to hyperemic flow rates. The recirculation zones are analyzed by plotting WSS contour and velocity vector at times of accelerating, peak and decelerating flows. The pressure drop from the inlet to the exit of the stent is also plotted to obtain a better understanding of the flow.

3.1 Velocity Profiles

To understand the nature of flow, axial velocity profiles are plotted along the radius of the artery at strut intersections and midpoints. The velocity profiles are plotted for basal to hyperemic flow rates at different time points, which represents acceleration, peak and deceleration flows. Figure 6 shows the axial velocity profiles at strut intersection 1 plotted along the radius of the artery i.e. from the center of the artery to the vessel wall, where radius of 0.125 cm represents the point of strut intersection (strut cross-link). The peak velocity ($u_{P_{1A}}, u_{P_{1B}}, u_{P_{1C}}$ and $u_{P_{1D}}$) during the entire cardiac cycle is observed to occur near the strut intersection for all flow rates. This happens due to the developing nature of the flow associated with uniform spatial distribution of inlet velocity. The peak velocity for the basal flow rate ($\tilde{Q}$ = 50 ml/min) is 33.7 cm/s, 27.4 cm/s, 16.3 cm/s and 11.3 cm/s at t = 2.00 s, 2.20 s, 1.85 s and 2.30 s, respectively (Figure 6A). As expected for hyperemic flow rate ($\tilde{Q}$ = 200 ml/min), the peak velocity is 4 times that of basal flow rate ($u_{P_{1D}}$ = 4 $u_{P_{1A}}$). The peak velocity for hyperemic flow rate is 136.1 cm/s, 112.5 cm/s, 65.8 cm/s and 37.3 cm/s at t = 2.00 s, 2.20 s, 1.85 s, and 2.30 s, respectively (Figure 6D). Also, the mean velocity of 73.9 cm/s for hyperemic flow rate is found to be 4 times the mean velocity of 18.2 cm/s for basal flow rate. The location of peak velocity, measured from the centerline of the artery lumen for basal flow rate is at 0.096 cm (L_{1A}). As the flow rate increases, the location of peak velocity shifts towards the wall ($L_{1A} < L_{1B} < L_{1C} < L_{1D}$) showing a sharper velocity gradient near the strut intersection, which creates a higher WSS as flow rate increased. The locations of peak velocity for $\tilde{Q}$ = 100 ml/min, 150 ml/min and 200 ml/min are at 0.1 cm (L_{1B}), 0.104 cm (L_{1C}), and 0.106 cm (L_{1D}), respectively.

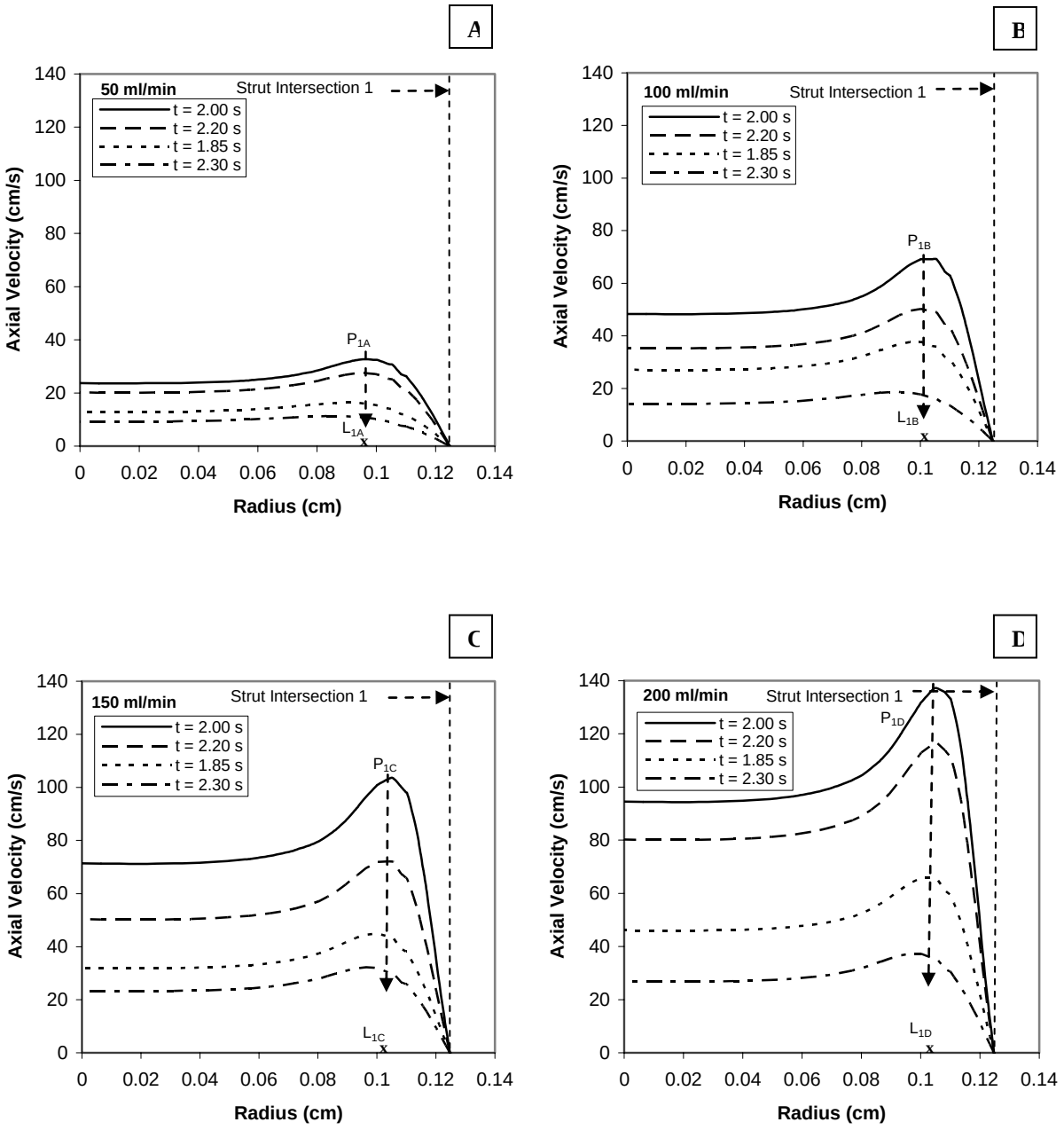

Figure 6. Variation of Axial Velocity along the Radius of the Artery at Intersection 1

As the flow develops from strut intersection 1 to strut intersection 2 (Figure 7), there is an average decrease of 5% in peak velocity. The peak velocity during the entire cardiac cycle occurs near the strut intersection except for basal flow rate where the peak velocity ($u_{p_{2A}}$) occurs at the center (X-axis) of the artery. The peak velocities for basal to hyperemic flow rates ($\tilde{Q}$ = 50 ml/min to 200 ml/min) are 31.8 cm/s, 65.4 cm/s, 96.8 cm/s, and 127.5 cm/s, respectively at t = 2.0 s. The velocity profile almost becomes parabolic for basal flow, showing that the flow is developing from strut intersection 1 to 2. Similar to strut intersection 1, increase in peak velocity and shift in location of peak velocity towards the wall from basal to hyperemic flow rates are observed at strut intersection 2. The location of peak velocity shifts towards the center as the flow proceeds from strut intersection 1 to 2 showing an average decrease of 50% in the velocity gradient, which leads to the reduction of WSS from strut intersection 1 to 2. At strut intersection 2, the locations of peak velocity for $\tilde{Q}$ = 50 ml/min, 100 ml/min, 150 ml/min and 200 ml/min are at axis (L_{2A}), 0.072 cm (L_{2B}), 0.076 cm (L_{2C}), and 0.077 cm (L_{2D}), respectively.

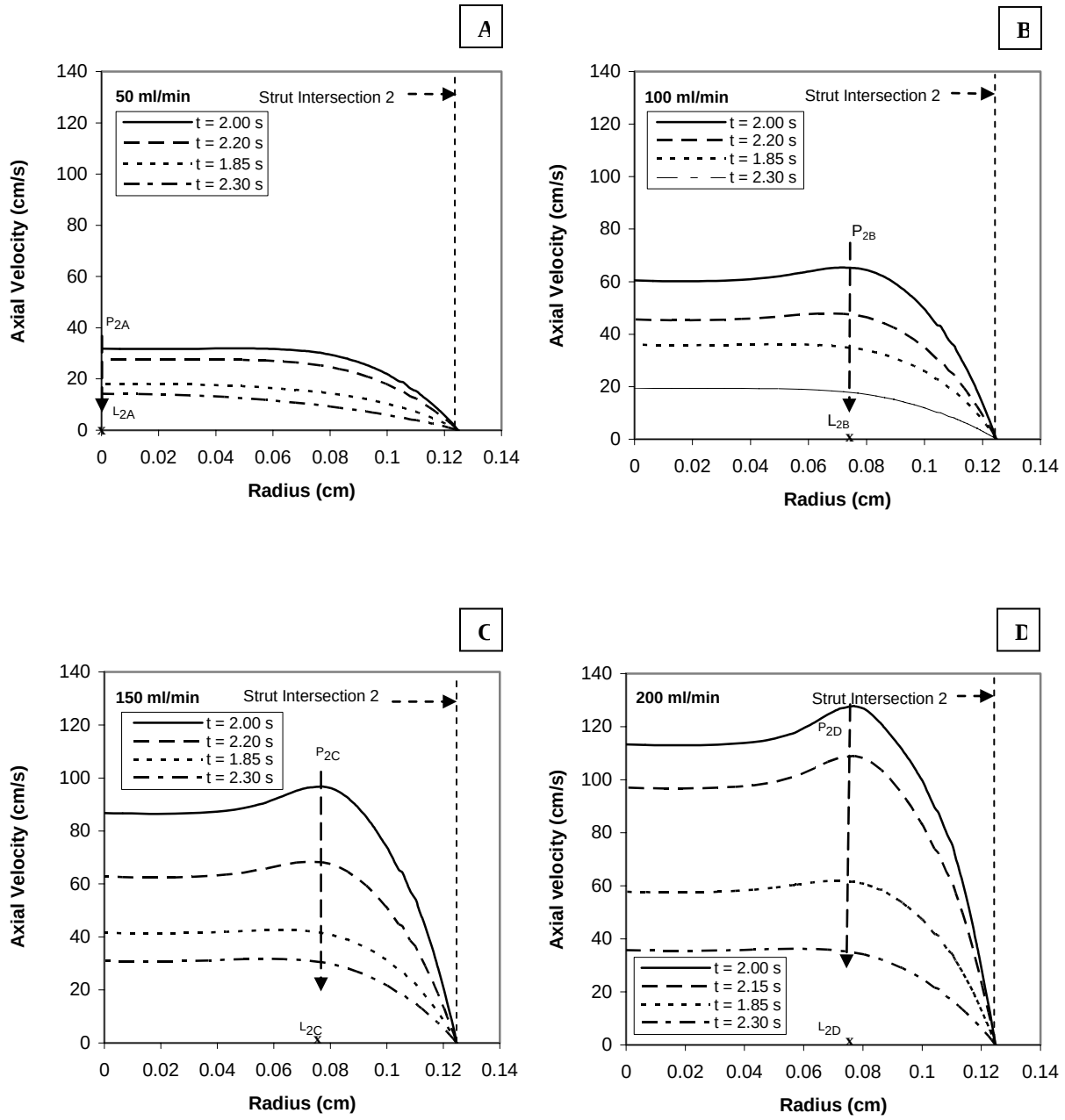

Figure 7. Variation of Axial Velocity along the Radius of the Artery at Intersection 2

As the flow further develops to the strut intersection 3 (Figure 8), the velocity profile becomes parabolic for 100 ml/min and 50 ml/min flow rates where the peak velocity occurs at the center of the artery. For lower flow rates, the flow gets developed earlier along the axial distance as the inlet velocities are low for basal flow as compared to hyperemic flow. The flow at strut intersection 3 is not fully developed for 150 ml/min and 200 ml/min flow rates where the peak velocity still occurs near the strut intersection. There is an average increase of 4% in peak velocity showing that the flow is developing from strut intersection 2 to 3. At strut intersection 3, the peak velocities for basal to hyperemic flow rates ($\tilde{Q}$ = 50 ml/min to 200 ml/min) are 35 cm/s, 66.9 cm/s, 97.6 cm/s, and 127.8 cm/s, respectively at t = 2.0 s. The location of peak velocity shifts towards the center as the blood flows from strut intersection 2 to 3 showing an average decrease of 28% in the velocity gradient. At strut intersection 3, the locations of peak velocity for $\tilde{Q}$ = 50 ml/min, 100 ml/min, 150 ml/min and 200 ml/min are at axis (L_{3A}), 0.049 cm (L_{3B}), 0.064 cm (L_{3C}), and 0.064 cm (L_{3D}), respectively.

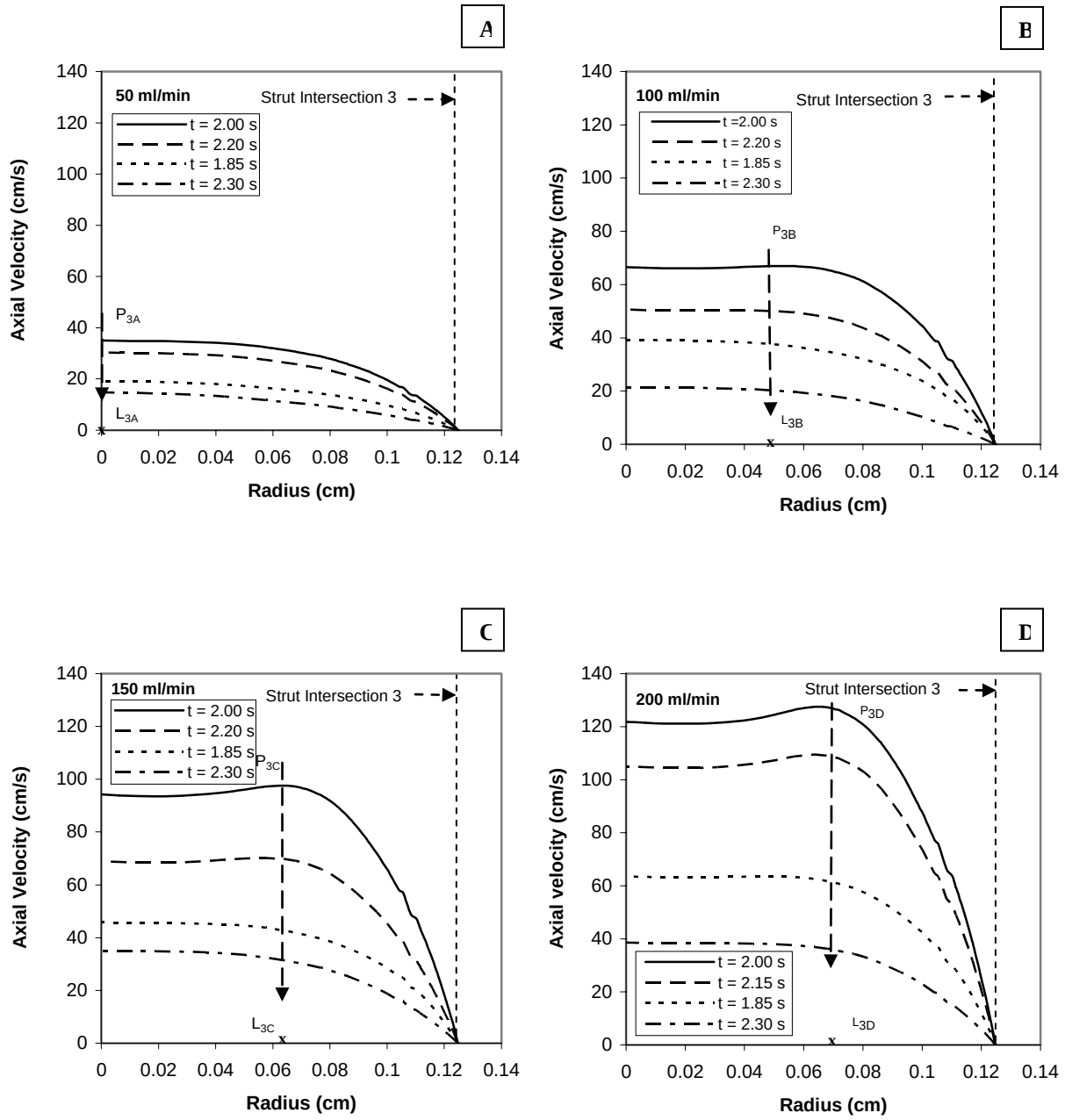

Figure 8. Variation of Axial Velocity along the Radius of the Artery at Intersection 3

As the flow reaches strut intersection 4 (Figure 9), a parabolic or nearly developed velocity profile is observed for 50, 100 and 150 ml/min flow rates, showing that the flow is developed for lower flow rates. The peak velocity ($u_{P_{4A}}$, $u_{P_{4B}}$ and $u_{P_{4C}}$) occurs at the center of the artery (L_{4B} = 0, L_{4C} = 0 and L_{4C} = 0). There is an average of 20% drop in the velocity gradient and 4% increase in peak velocity from strut intersection 3 to 4. At strut intersection 4, the peak velocities for basal to hyperemic flow rates ($\tilde{Q}$ = 50 ml/min to 200 ml/min) are 36.5 cm/s, 70.48 cm/s, 100 cm/s, and 130.3 cm/s, respectively at t = 2.0 s. The slope of the velocity curve between the wall and the location of peak velocity is sharp for strut intersection 1. The velocity gradient decreases along the struts, implying that the WSS value decreases with each subsequent axial strut location along the flow direction. At strut intersection 4, the locations of peak velocity for $\tilde{Q}$ = 50 ml/min, 100 ml/min and 150 ml/min are at axis. For hyperemic flow rate, the location of peak velocity is at 0.057 cm (L_{4D}) showing that the flow is not yet developed. Thus, the developing nature of the flow is observed as the flow proceeds from strut intersection 1 where the peak velocity occurs near the wall to strut intersection 4 where the peak velocity occurs at the centre of the artery.

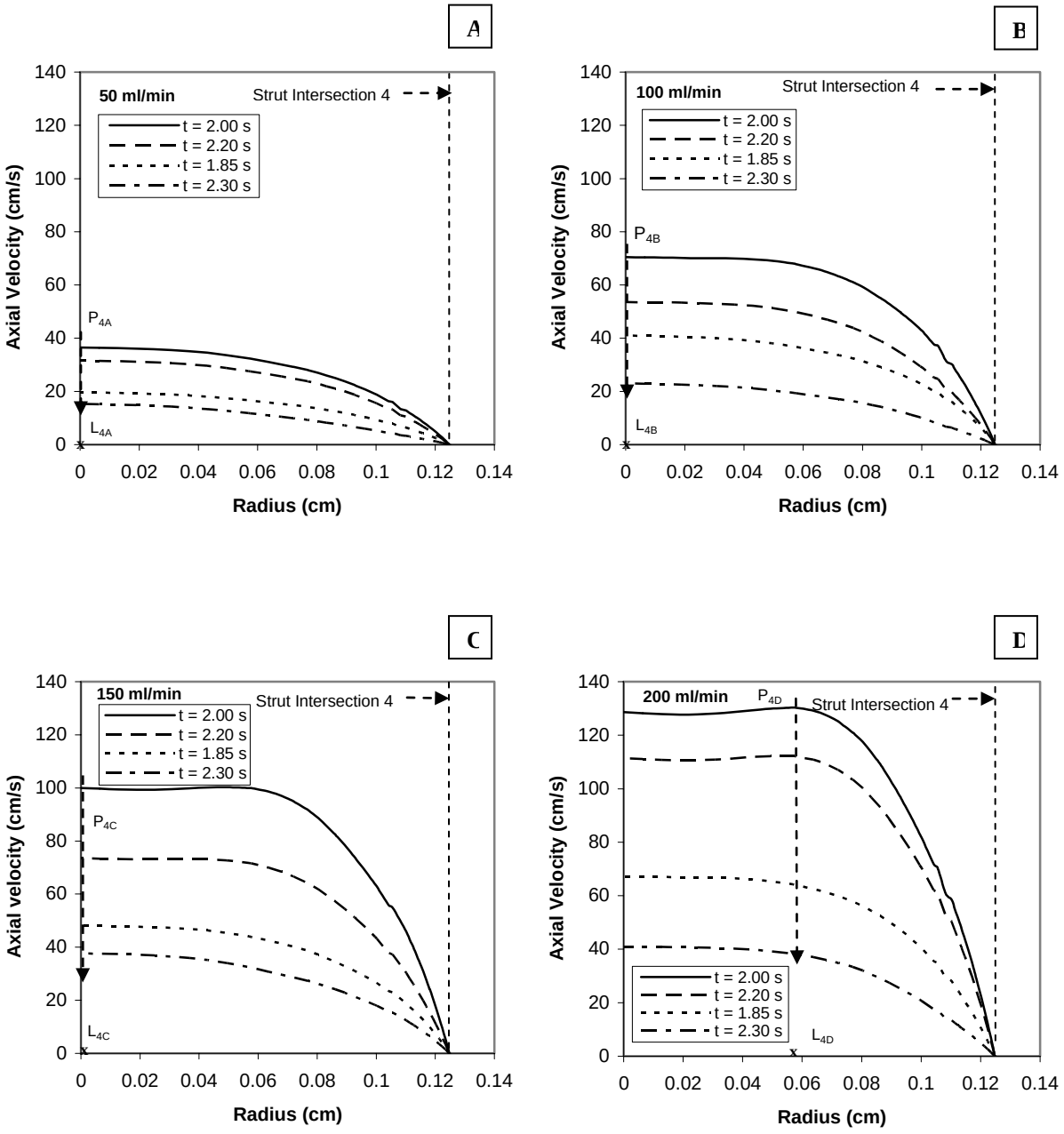

Figure 9. Variation of Axial Velocity along the Radius of the Artery at Intersection 4

Figure 10 shows the variation of axial velocity at midpoint 1 i.e. at the central location of the void space between the strut intersections 1 and 2. Here, a velocity profile similar to the profile at the entrance region i.e. at strut intersection 1 is observed. The peak velocity ($u_{Q_{1A}}, u_{Q_{1B}}, u_{Q_{1C}}$ and $u_{Q_{1D}}$) during the entire cardiac cycle occurs near the arterial wall for all the flow rates. As the flow rate increases from basal to hyperemic, location of peak velocity shifts towards the wall ($N_{1A} < N_{1B} < N_{1C} < N_{1D}$) showing a high velocity gradient between the wall and the location of peak velocity for higher flow rates. When the flow proceeds from intersection 1 to midpoint 1, the location of peak velocity shifts towards the center of the artery ($N_{1A\text{-}1D} < L_{1A\text{-}1D}$), showing an average of 48% drop in the velocity gradient which results in reduced WSS value at midpoint compared to that at intersection points. At midpoint 1, the locations of peak velocity for $\tilde{Q}$ = 50 ml/min, 100 ml/min, 150 ml/min and 200 ml/min are at 0.067 (N_{1A}), 0.081 cm (N_{1B}), 0.085 cm (N_{1C}), and 0.088 cm (N_{1D}). There is an average of 6% decrease in peak velocity ($u_{Q_{1A-1D}} < u_{P_{1A-1D}}$) from intersection 1 to midpoint 1. At midpoint 1, the peak velocities for basal to hyperemic flow rates ($\tilde{Q}$ = 50 ml/min to 200 ml/min) are 30.5 cm/s, 64.2 cm/s, 96.1 cm/s, and 129.6 cm/s, respectively at t = 2.0 s.

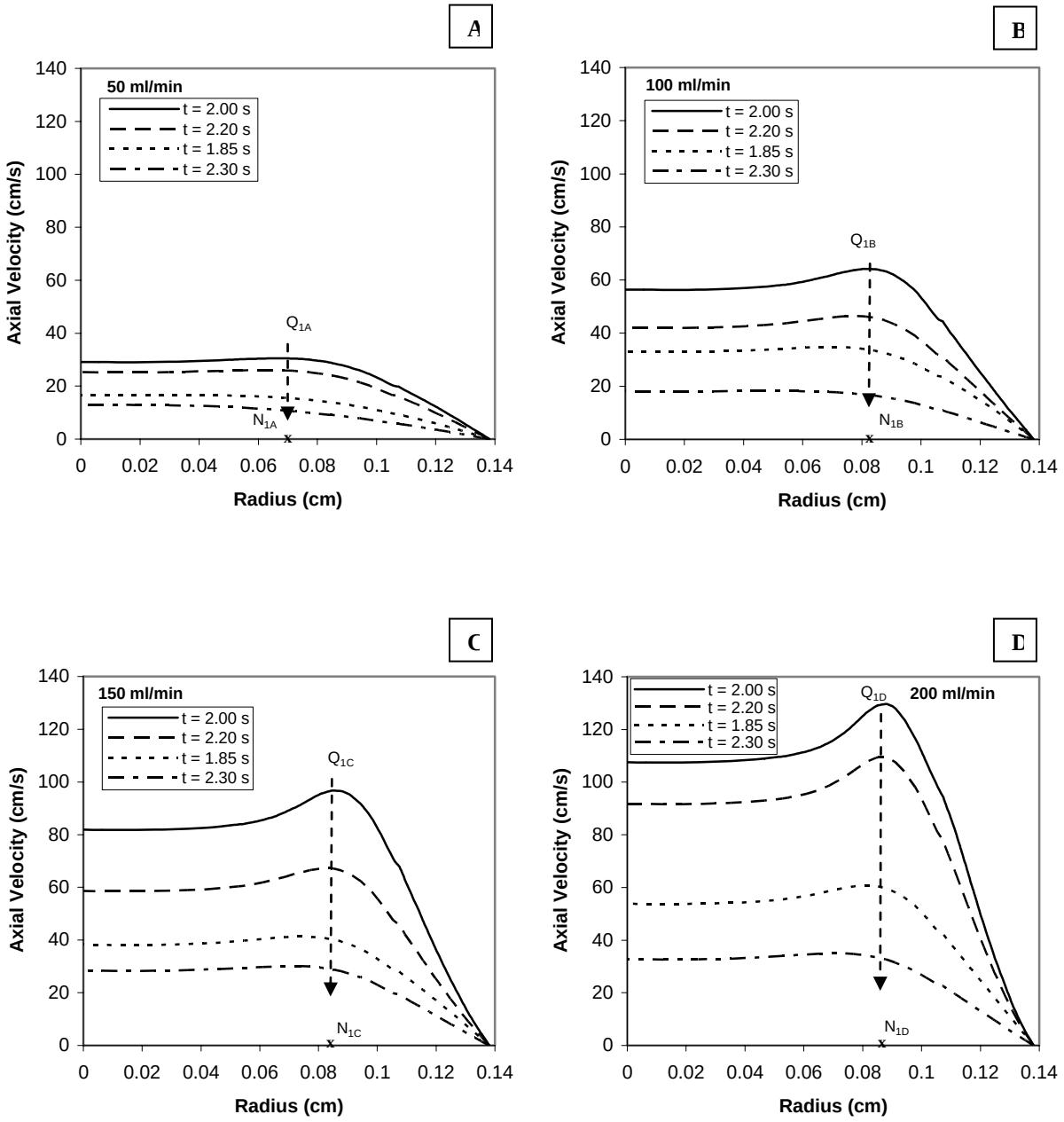

Figure 10. Variation of Axial Velocity along the Radius of the Artery at Midpoint 1

As the flow develops, the velocity profile starts becoming more developed and eventually parabolic for basal flow rate at midpoint 2 (Figure 11) where the peak velocity occurs at the center of the artery. For all other flow rates, the peak velocity occurs near the arterial wall. The location of peak velocity shifts towards the center of the artery from midpoint 1 to 2 showing an average of 28% drop in the velocity gradient. At midpoint 2, the locations of peak velocity for $\tilde{Q}$ = 50 ml/min, 100 ml/min, 150 ml/min and 200 ml/min are at axis (N_{2A}), 0.058 cm (N_{2B}), 0.069 cm (N_{2C}), and 0.074 cm (N_{2D}), respectively. There is an average increase of 4% in peak velocity from midpoints 1 to 2. At midpoint 2, the peak velocities for basal to hyperemic flow rates ($\tilde{Q}$ = 50 ml/min to 200 ml/min) are 33.6 cm/s, 65.3 cm/s, 96.7 cm/s, and 126.5 cm/s, respectively at t = 2.0 s.

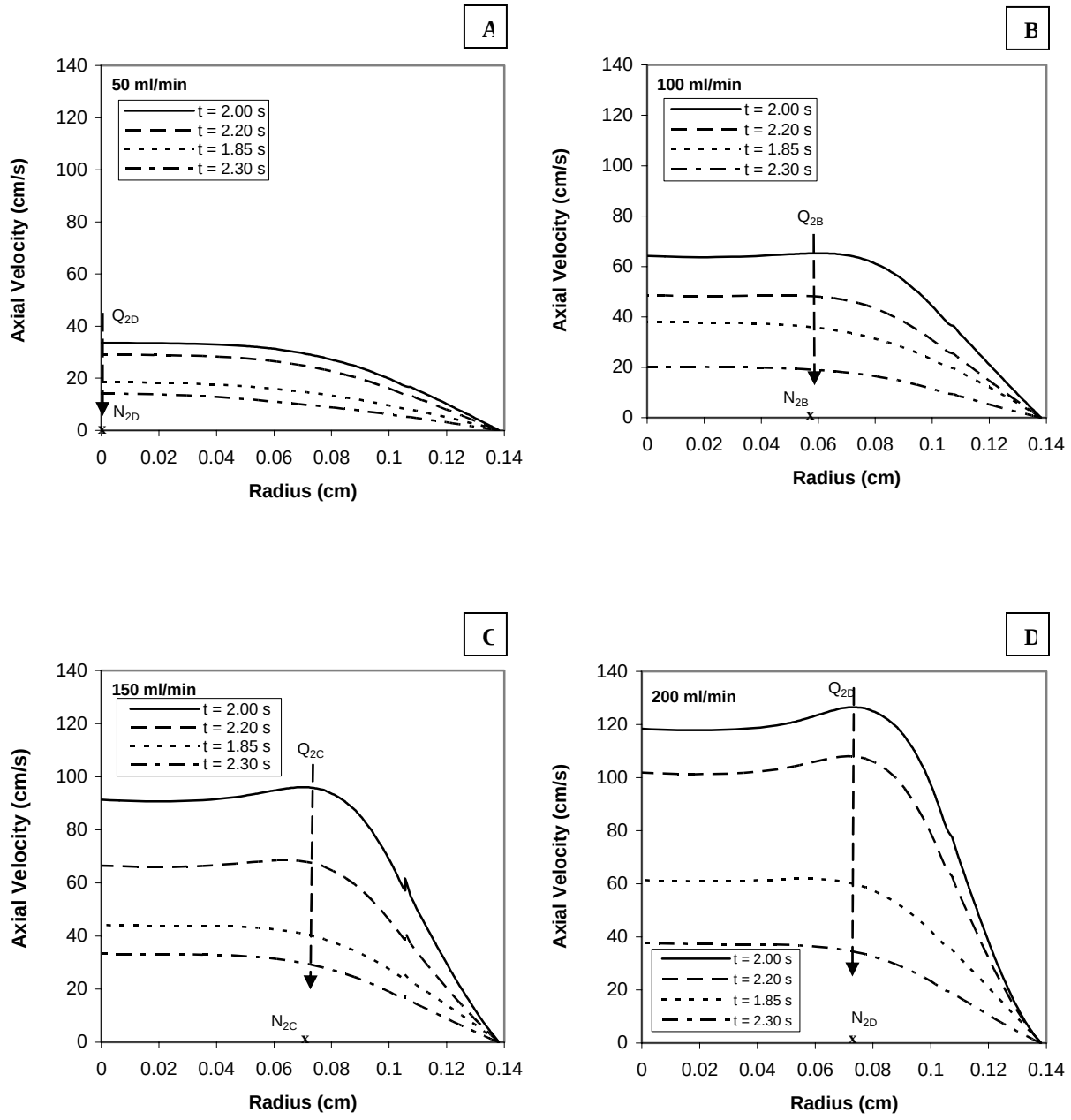

Figure 11. Variation of Axial Velocity along the Radius of the Artery at Midpoint 2

As the flow reaches the midpoint 3, a smoother parabolic velocity profile is seen for 50 and 100 ml/min flow rates at midpoint 3 (Figure 12) showing that the flow is developed and near parabolic where the peak velocity occurs ($u_{Q_{3A}}$ and $u_{Q_{3B}}$) at the center. The location of peak velocity shifts towards the center of the artery as the flow proceeds from midpoint 2 to 3 showing an average of 23% drop in the velocity gradient. At midpoint 3, the locations of peak velocity for $\tilde{Q}$ = 50 ml/min and 100 ml/min are at axis (N_{3A} and N_{3B}). The locations of peak velocity for $\tilde{Q}$ = 150 ml/min and 200 ml/min are at 0.054 cm (N_{3C}), and 0.061 cm (N_{3D}), respectively. There is an average increase of 3.7% in peak velocity from midpoints 2 to 3. At midpoint 3, the peak velocities for basal to hyperemic flow rates ($\tilde{Q}$ = 50 ml/min to 200 ml/min) are 35.5 cm/s, 68.8 cm/s, 98.32 cm/s, and 128.6 cm/s, respectively at t = 2.0 s. The developing flow profile is clearly seen from the entrance region of the stented artery where the maximum peak velocity occurs near the strut intersection to the exit of the artery where the velocity profile is more developed and near parabolic.

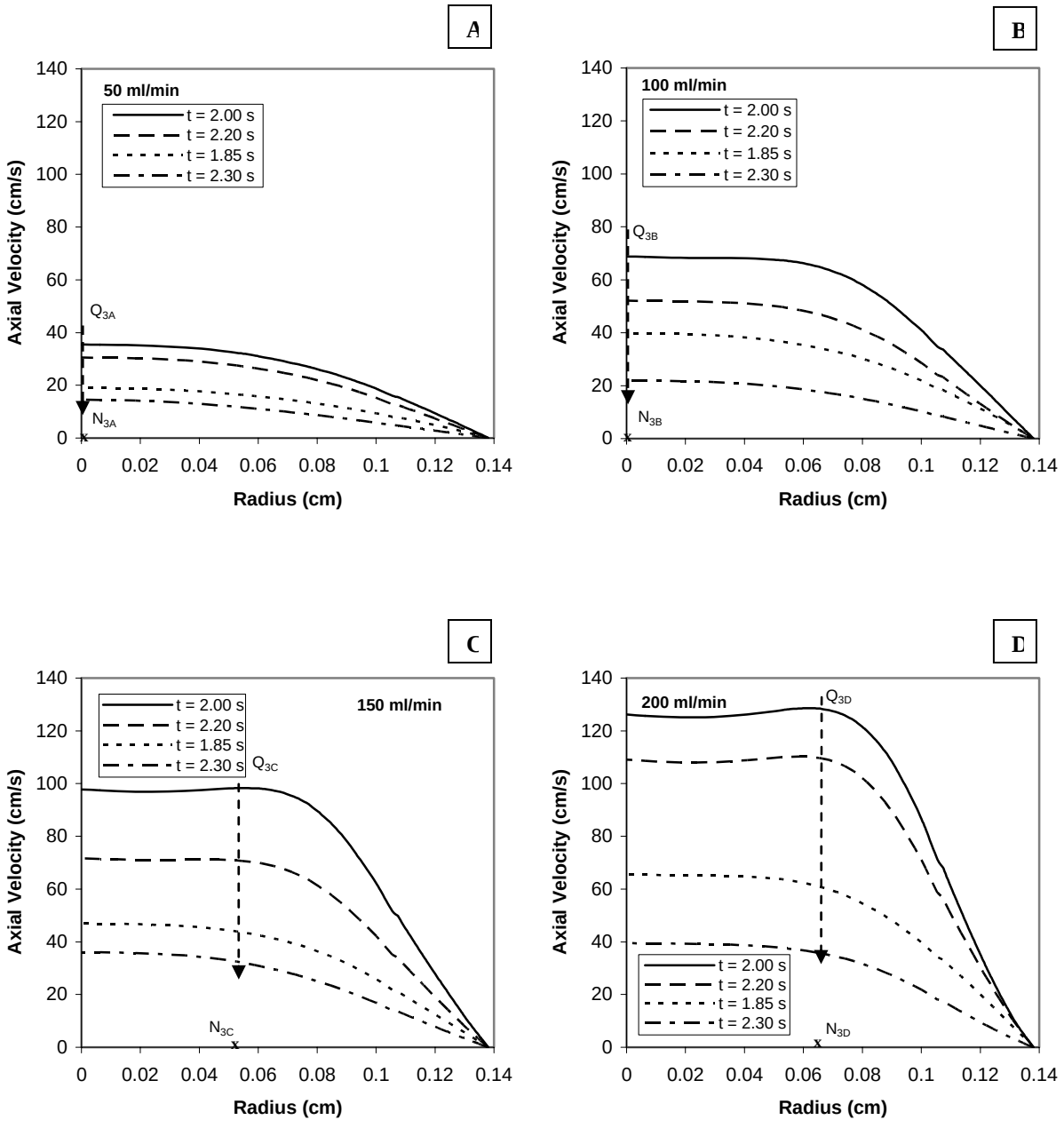

Figure 12. Variation of Axial Velocity along the Radius of the Artery at Midpoint 3

3.2 Wall Shear Stress Distributions

The pulsatile flow is analyzed along the entire length of the artery by plotting the WSS at various points inside the stented arterial domain shown in Figure 5. Since WSS is the resultant of x, y and z components of wall shear stress which results in a positive value, axial wall shear stress is plotted in order to identify regions of negative WSS showing the recirculation zones. Figure 13 shows the phasic variation of axial WSS at the strut intersections 1 to 4 for basal to hyperemic flow rates. For the pulse cycle the WSS attained its peak value at peak diastole (t = 2.00 s). Maximum WSS occurs at the entrance region of the stent (strut intersection 1) which is due to the developing nature of the flow at the inlet. As the flow develops along the stent, there is a predominant reduction in maximum WSS about 40% to 50% from strut intersection 1 to strut intersection 4 (along R_A, R_B, R_C and R_D) as the velocity gradient at the wall decreases along the axial flow direction. There is a significant reduction in WSS from strut intersection 1 to 2 and then a modest decrease along the subsequent strut locations. Peak value of WSS for basal flow rate is 90 dyn/cm^2 near the entrance of the stent. It increases to 195.45 dyn/cm^2 for Q = 100 ml/min, 285.19 dyn/cm^2 for Q = 150 ml/min, 360 dyn/cm^2 for hyperemic flow rate which is about 25 times higher than the normal time-mean value of 12 dyn/cm^2. On average the maximum WSS for hyperemic flow rate is about 4 times that at basal flow rate ($\tau_{R_D} \approx 4\tau_{R_A}$).

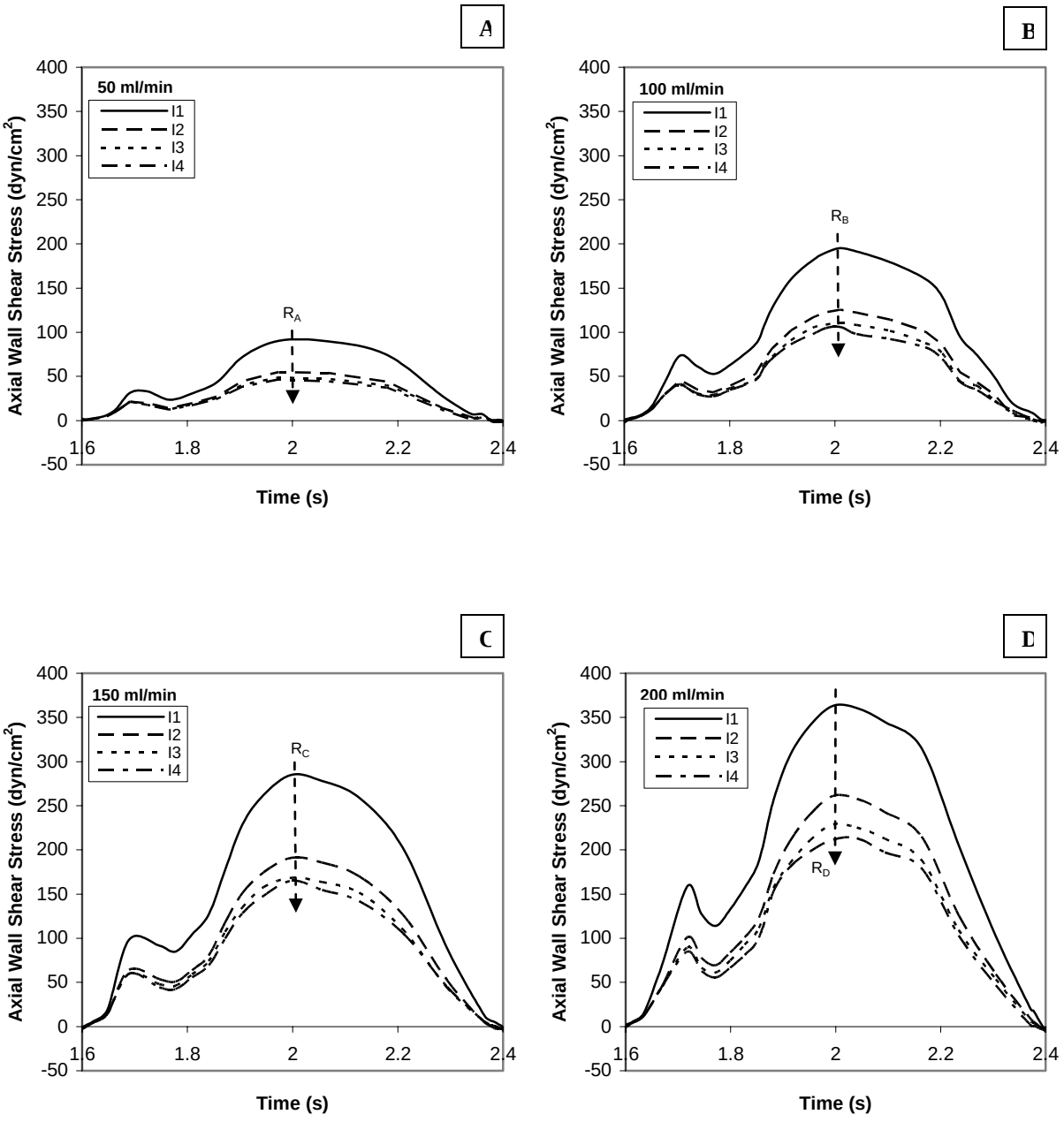

Figure 13. Temporal Variation of Wall Shear Stress at Strut Intersections (I)

In order to study the effect of stent on wall shear stress distributions, WSS is plotted at the void spaces between the stent struts. Stent geometry shows a significant effect on WSS distributions. A significant reduction in WSS is observed at midpoints between two adjacent strut intersections from WSS values at strut intersections. Figure 14 shows the phasic variation of axial WSS at the midpoints 1 to 3 for basal to hyperemic flow rates. Peak value of WSS at midpoints reduces by 1/3rd (τ_{R_E} = 1/3 τ_{R_A}) and 1/6th (τ_{R_H} = 1/6 τ_{R_D}) of that at strut intersections for basal and hyperemic flow rates, respectively as the velocity gradient at midpoint is considerably lower than that at strut intresections. Peak value of WSS occurs near the entrance region of the stent, midpoint 1. Peak stress at midpoint 1 is 27.86 dyn/cm^2 for basal flow rate which increases to 50.26 for Q = 100 ml/min, 59.02 dyn/cm^2 for Q = 150 ml/min, 61.8 dyn/cm^2 for hyperemic flow rate. As the flow develops along the stent, there is an average of 16% reduction in peak WSS from midpoint 1 to midpoint 3 (along R_E, R_F, R_G and R_H).

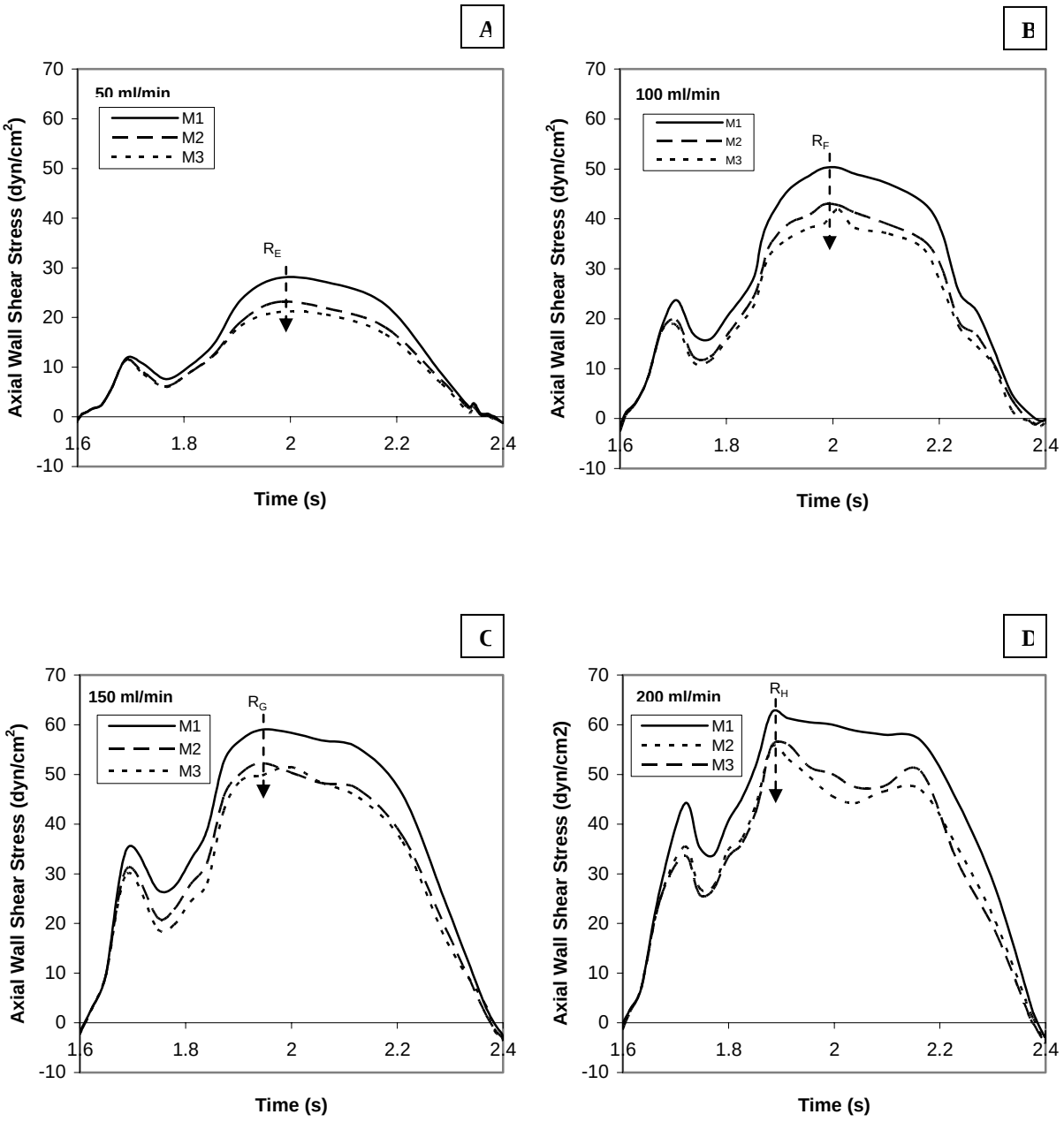

Figure 14. Temporal Variation of Wall Shear Stress at Strut Midpoints (M)

Figure 15 shows the phasic variation of axial WSS at the vertices 1 to 8. Vertices 1, 3, 5 and 7 represent the upstream and vertices 2, 4, 6 and 8 represent the downstream of strut intersections 1, 2, 3, and 4, respectively (Fig. 5). It can be observed that positive WSS occurs at the upstream and negative WSS at the downstream of strut intersections during most of the cardiac cycle for all flow rates, except for the basal flow rate where negative shear stress occurs even at the upstream location of strut intersection 1. At the end of the pulse cycle, negative shear stress is observed at the upstream of strut intersections due to the flow reversal taking place near the arterial wall. It can be inferred that recirculation zones exist at the downstream of each strut intersection. Maximum WSS values, both positive and negative occur near the entrance of the stent, at vertices 1 and 2, respectively. As the flow develops and reaches the strut intersection 4, maximum positive WSS decreases by a factor of 3.8 and maximum negative WSS decreases by 26% in magnitude. As the flow rate increases from basal to hyperemic, the maximum positive shear stress increases from 0.76 dyn/cm^2 to 57.19 dyn/cm^2, 75 times the basal value and the negative shear stress increases from -1.36 dyn/cm^2 to -7.16 dyn/cm^2, around 5 times the basal value in magnitude. The increase in the magnitude of negative WSS shows a higher recirculation for higher flow rates.

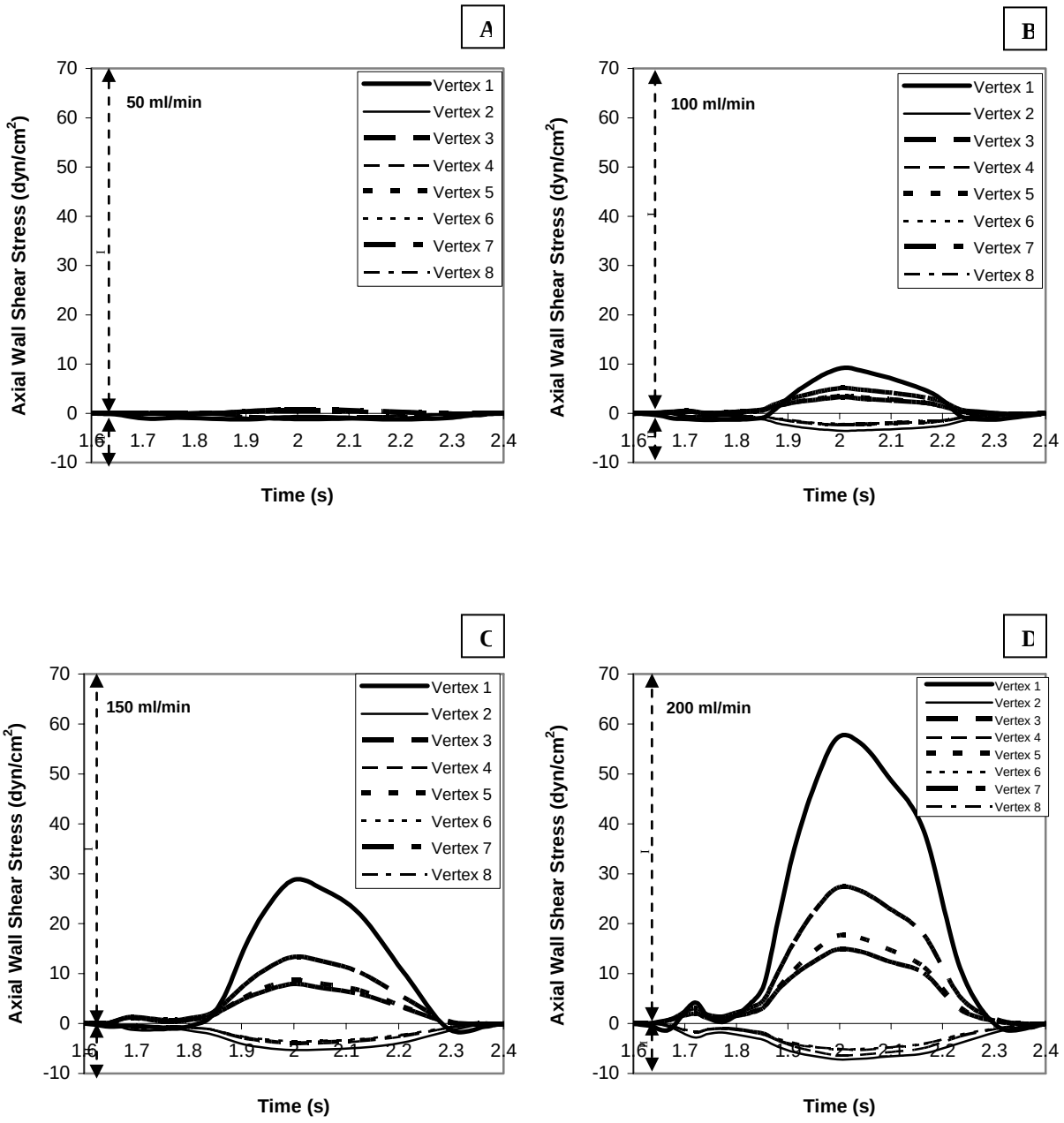

Figure 15. Temporal Variation of Wall Shear Stress at Vertices. I – Upstream of strut intersection, II – Downstream of strut intersection

Figure 16 shows the axial variation of WSS along the artery wall for basal to hyperemic flow rates at times of accelerating, peak and decelerating flows. Due to the developing nature of the flow at the inlet, the WSS value is very high of around 530 dyn/cm^2 near the entrance i.e., just upstream of the top of the strut cross-link (intersection) 1 for hyperemic flow, and as the flow develops, there is a significant reduction (~56%) of peak positive shear stress to 230 dyn/cm^2 at strut intersection 4. Between strut intersection 1 and 2 for hyperemic flow, the WSS increases in the flow direction from -10 dyn/cm^2 to 120 dyn/cm^2 which is caused by the reattachment of the developing flow. Subsequently, there is a decrease in shear stress to 10 dyn/cm^2 at the upstream (UP) of strut intersection due to flow stagnation. Axially downstream there is a sharp increase to a very high WSS of around 300 dyn/cm^2 at the strut intersection 2 (ST) followed by a sharp fall to a negative WSS at the immediate downstream (DS) of the strut intersection. From strut intersections 1 to 4, the peak positive WSS decreases from 105.85 dyn/cm^2 to 49.04 dyn/cm^2 for basal flow, from 258.34 dyn/cm^2 to 117.49 dyn/cm^2 for Q = 100 ml/min, and from 397.25 dyn/cm^2 to 186.87 dyn/cm^2 for Q = 150 ml/min. Similar variation in WSS distributions is found in the work of LaDisa et al. [26] except the negative WSS at the downstream of strut intersection.

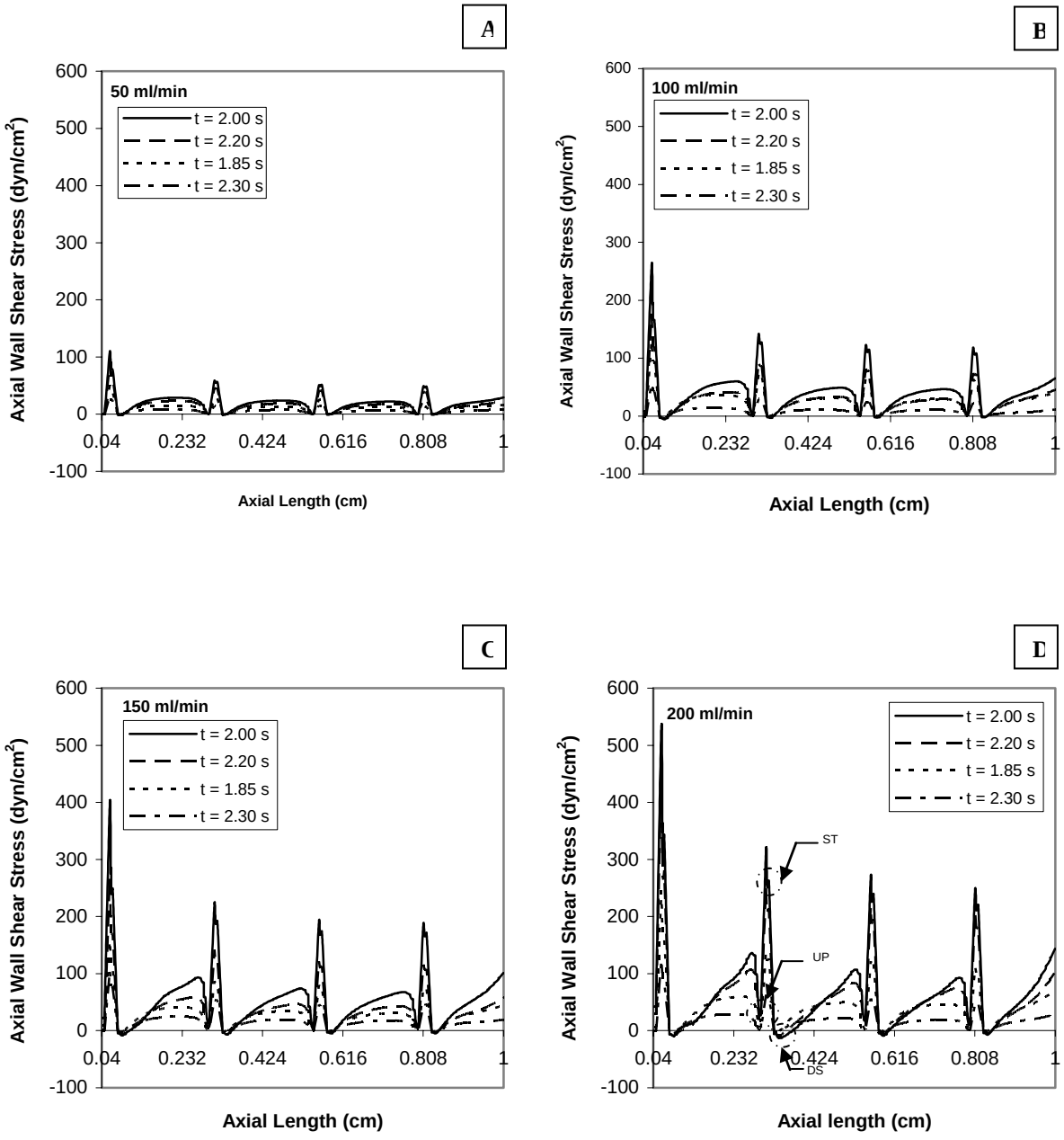

Figure 16. Axial Variation of Wall Shear Stress Along the Artery Wall

The presence of stent struts not only increases the WSS to a very high peak value but also leads to the formation of a recirculation zone at the immediate downstream of strut intersection. Past studies suggest that alterations in local WSS distributions inside the vessel may affect the endothelial cell response, an important component of intimal hyperplasia (Edelman and Rogers [21]). Intimal hyperplasia had been noted at the proximal and distal ends of implanted stents which leads to a qualitative conclusion that altered distributions of WSS may be a contributing factor to restenosis. The results from the present study support the contention that stent geometry following deployment alters the WSS distributions, which in turn, may represent one of the contributing factors to restenosis.

3.3 Modified Oscillatory Shear Index (MOSI)

Figure 17 shows the variation of modified oscillatory shear index with flow rate. To analyze the flow inside the stent, MOSI is plotted at upstream and downstream of each strut intersection (vertices 1 to 8) from basal to hyperemic flow rates. Fig. 17 shows a positive WSS during the entire cardiac cycle at the upstream of each strut intersection for all flow rates except for basal flow rate where there is a negative WSS near the entrance (vertex 1), and a negative WSS at the downstream of each strut intersection for all flow rates. This implies that there is a persistent recirculation at the downstream of each strut intersection.

It is evident from the figs. 6-8 that zones of flow stagnation and recirculation are formed at the immediate upstream and downstream of each strut intersection, respectively. In line with these results, previous results show that large amounts of dye accumulated between adjacent struts (Berry et al. [8]).

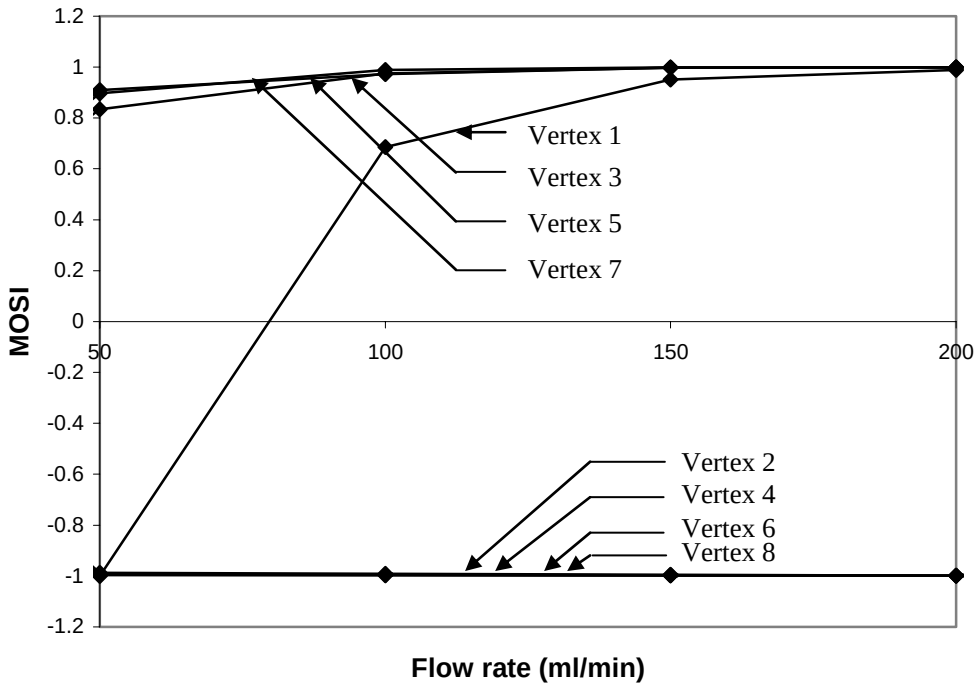

Figure 17. Variation of Modified OSI with Flow Rate at Vertices

3.4 Recirculation Zones

To estimate the recirculation zones, WSS contour is plotted for basal to hyperemic flow rates. Figure 18 shows the contour plot of axial WSS for basal flow rate at times of accelerating, peak and decelerating flows. In order to identify the zones of recirculation, negative axial WSS is plotted. It can be observed that recirculation zones are formed only at the proximate regions of each strut intersection (strut cross-link). Very small recirculation zones are formed for basal flow at the downstream, right and left side of each strut intersection with high negative WSS in the region close to the strut cross-link and low negative WSS at the outer region of the recirculation zone. Maximum negative WSS is observed to occur near the entrance of the stent i.e. near strut intersection 1 due to the developing nature of the flow. Maximum negative WSS near the entrance is -1.29 dyn/cm^2 during the flow acceleration (t = 1.85 s), which increases to 7 dyn/cm^2 as the flow attains its peak velocity (t = 2.0 s). As the flow decelerates, there is a decrease of maximum negative WSS to -3.47 dyn/cm^2 at t = 2.20 s and then to -0.71 dyn/cm^2 at t = 2.30 s.

Figure 19 shows the contour plot of axial WSS for $\tilde{Q}$ = 100 ml/min at times of accelerating, peak and decelerating flows. Here, recirculation zones similar to those observed for basal flow are formed at the downstream, right and left side of each strut intersection of relatively larger in size. Maximum negative WSS near the entrance of the stent is -5.66 dyn/cm^2 during the flow acceleration (t = 1.85 s), which increases to 33.7 dyn/cm^2 at peak flow (t = 2.0 s). As the flow decelerates, the maximum negative WSS decreases to -17.55 dyn/cm^2 at t = 2.20 s and then further decreases to -2.27 dyn/cm^2 at t = 2.30 s.

As the flow rate increases, strange behavior of blood flow is noted. Unlike for lower flow rates ($\tilde{Q}$ = 50 ml/min and 100 ml/min) where three separate recirculation zones are formed at the

downstream, right and left side of each strut intersection, for $\tilde{Q}$ = 150 ml/min at peak flow (t = 2.0 s), the recirculation zones near the strut intersection 1 merge together and form a single recirculation zone along the strut (Fig. 20 B). The recirculation zones near strut intersections 2, 3, and 4 are separate zones similar to those formed for lower flow rates. Maximum negative WSS near strut intersection 1 is -13.66 dyn/cm^2 during the flow acceleration (t = 1.85 s), which increases to -98.4 dyn/cm^2 at peak flow where complex recirculation zones are formed. As the flow decelerates, there is a decrease of maximum negative WSS to -47.66 dyn/cm^2 at t = 2.20 s and then to -5.27 dyn/cm^2 at t = 2.30 s.

For hyperemic flow rate, larger recirculation zones are formed inside the stent as shown in figure 21. Merging of recirculation zones takes place near the entrance of the stent and this atypical flow behavior extends to strut intersection 2 at peak flow (Fig. 21B) due to high inlet velocity of 91.3 cm/s. As the flow decelerates, at t = 2.20 s, the recirculation zones get separated near the strut intersection 2 whereas, near the strut intersection 1, complex recirculation zones are still observed (Fig. 20C). The recirculation zones starts getting merged at peak flow and are completely merged at t = 2.20 s. As the flow decelerates further, at t = 2.30 s, distinct recirculation zones are formed near all strut intersections (Fig. 21D). Maximum negative WSS near the entrance of the stent is -28.18 dyn/cm^2 at t = 1.85 s and then increases to -200 dyn/cm^2 at peak flow. As the flow decelerates (t = 2.20 s), the recirculation zones starts getting separated where the maximum negative WSS near the entrance is -101.58 dyn/cm^2 and the WSS further gets reduced to -10.02 dyn/cm^2 at t = 2.30 s. The maximum negative WSS in a pulse cycle for hyperemic flow rate is about 28 times higher in magnitude than that for basal flow rate.

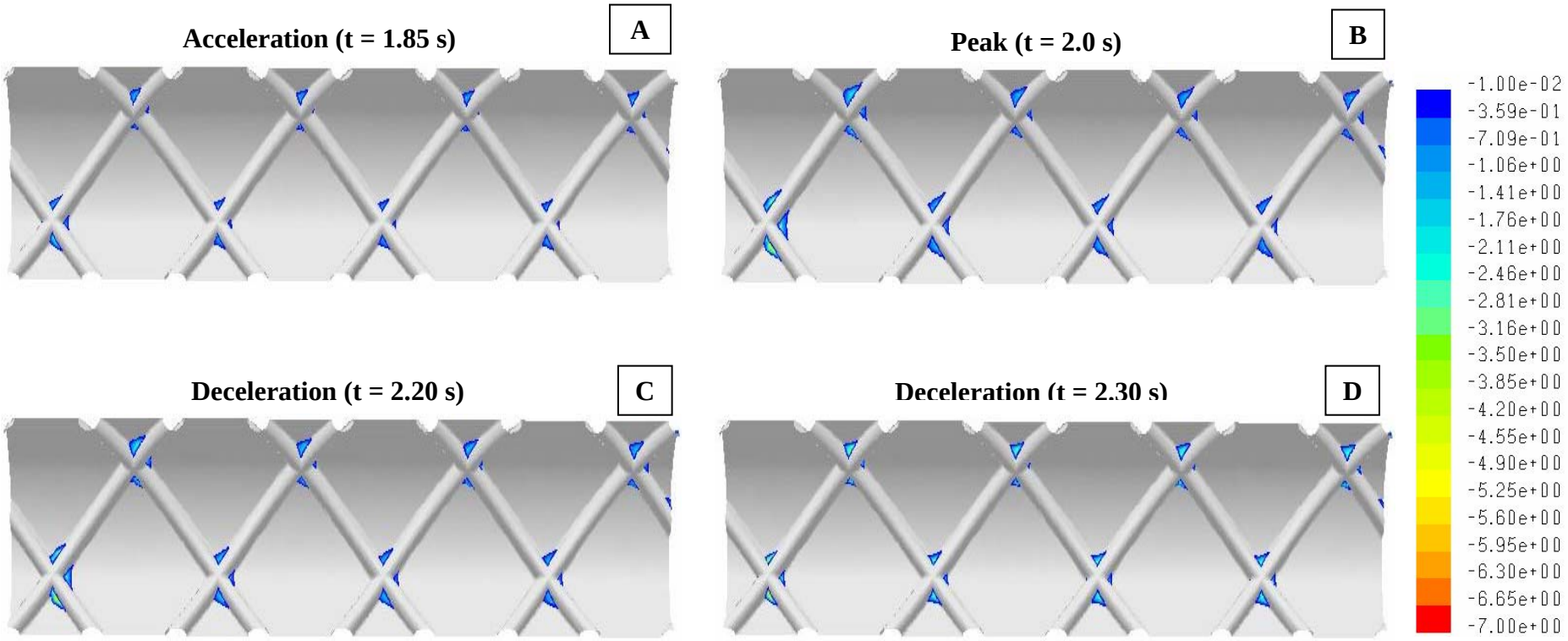

Figure 18. Contour Plot of Axial Wall Shear Stress Showing the Recirculation Zones for $\tilde{Q}$ = 50 ml/min at Times of Accelerating, Peak and Decelerating Flows

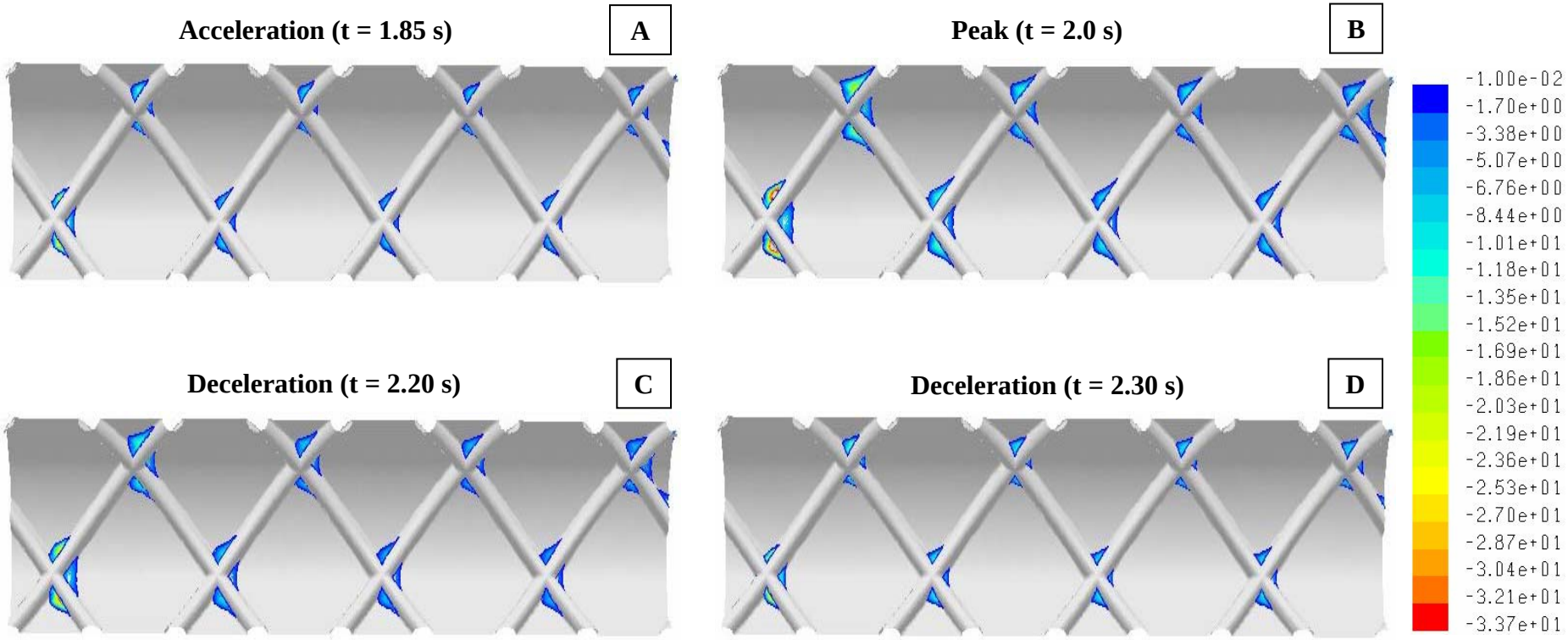

Figure 19. Contour Plot of Axial Wall Shear Stress Showing the Recirculation Zones for $\tilde{Q}$ = 100 ml/min at Times of Accelerating, Peak and Decelerating Flows

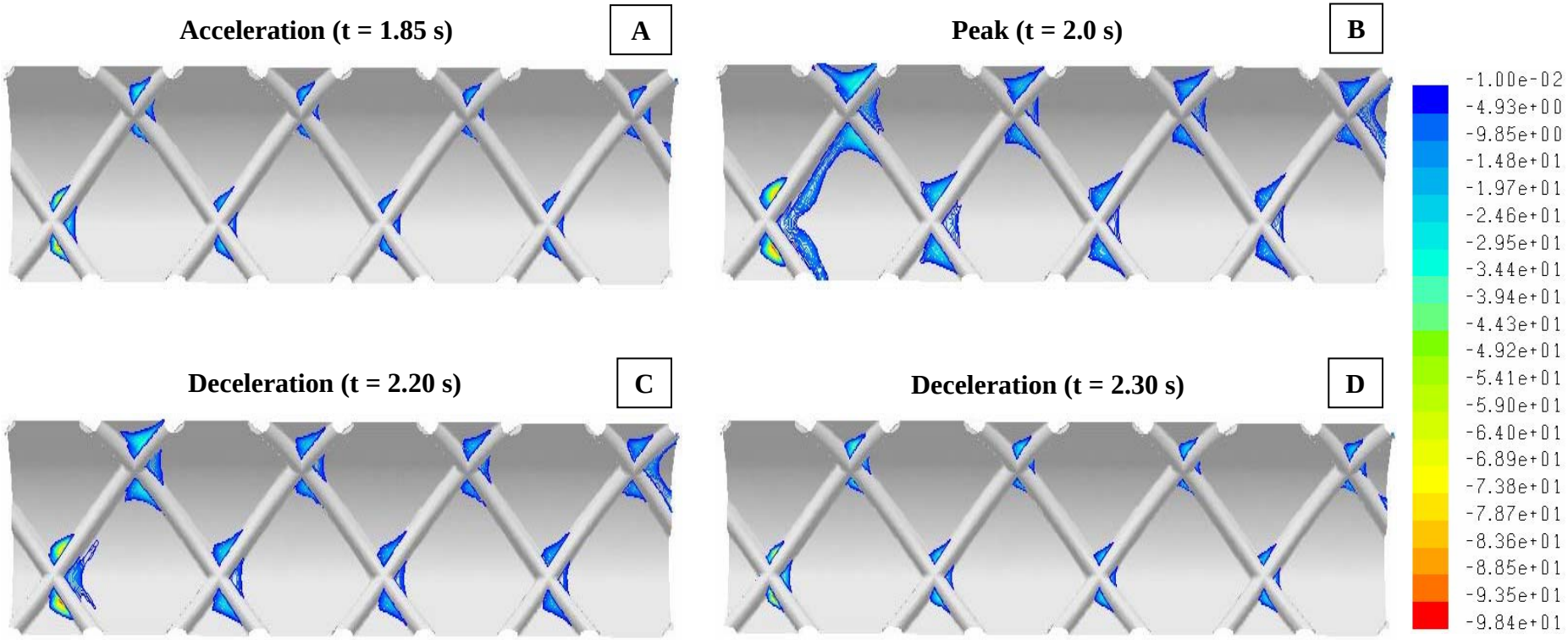

Figure 20. Contour Plot of Axial Wall Shear Stress Showing the Recirculation Zones for $\tilde{Q}$ = 150 ml/min at Times of Accelerating, Peak and Decelerating Flows

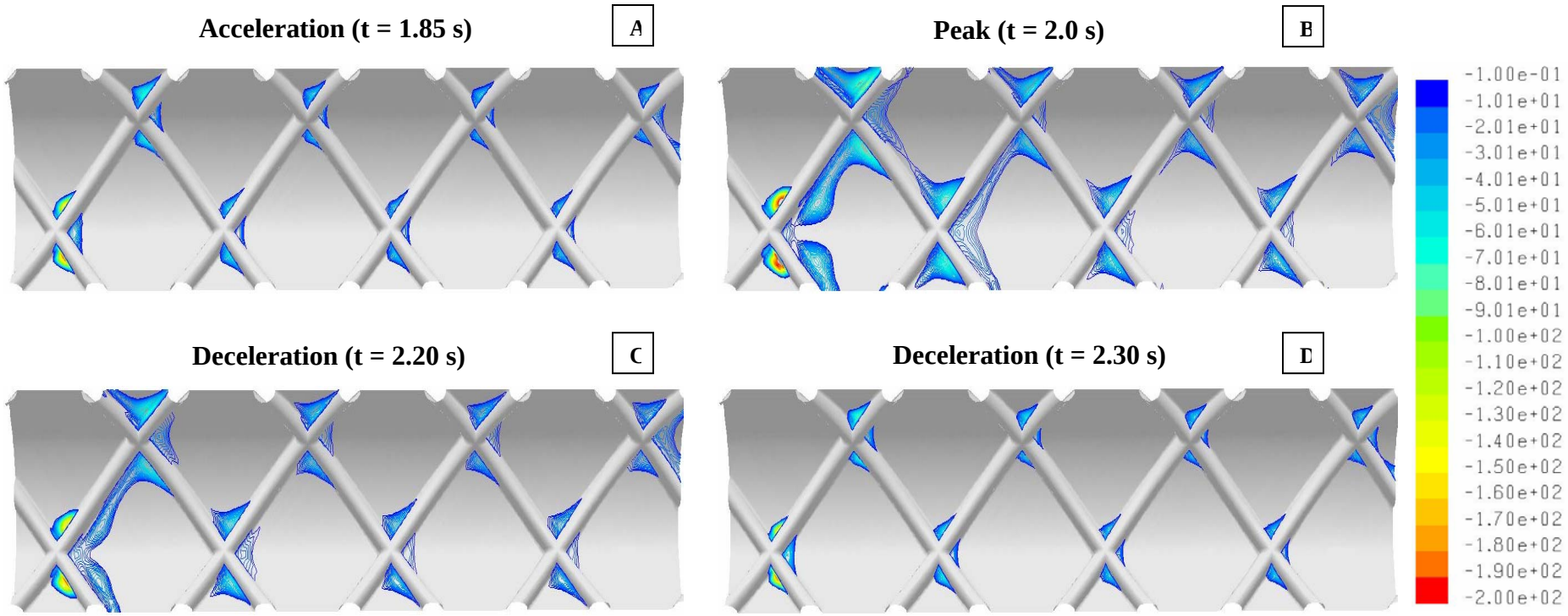

Figure 21. Contour Plot of Axial Wall Shear Stress Showing the Recirculation Zones for $\tilde{Q}$ = 200 ml/min at Times of Accelerating, Peak and Decelerating Flows

Figure 22 shows the velocity vector plotted near the immediate upstream and downstream of each strut intersection for hyperemic flow rate at peak flow (t = 2.0 s). Negative axial velocity vector is plotted to identify the zones of recirculation distinctly. It can be seen that small recirculation zones are formed at the immediate downstream of each strut intersection. The size of the recirculation zone near the strut intersection 2 (Fig. 22B) is larger than that near the strut intersection 1 (Fig. 22A). This type of flow behavior is similar to that observed in WSS contour plot (Fig. 21B) where the length of the recirculation zone at the immediate downstream of strut intersection 1 is smaller than that at the immediate downstream of strut intersection 2 as the recirculation zones are completely merged near strut intersection 2. As the flow proceeds along the struts, the size of recirculation zone decreases near the strut intersection 3 and further decreases as the flow reaches the strut intersection 4.

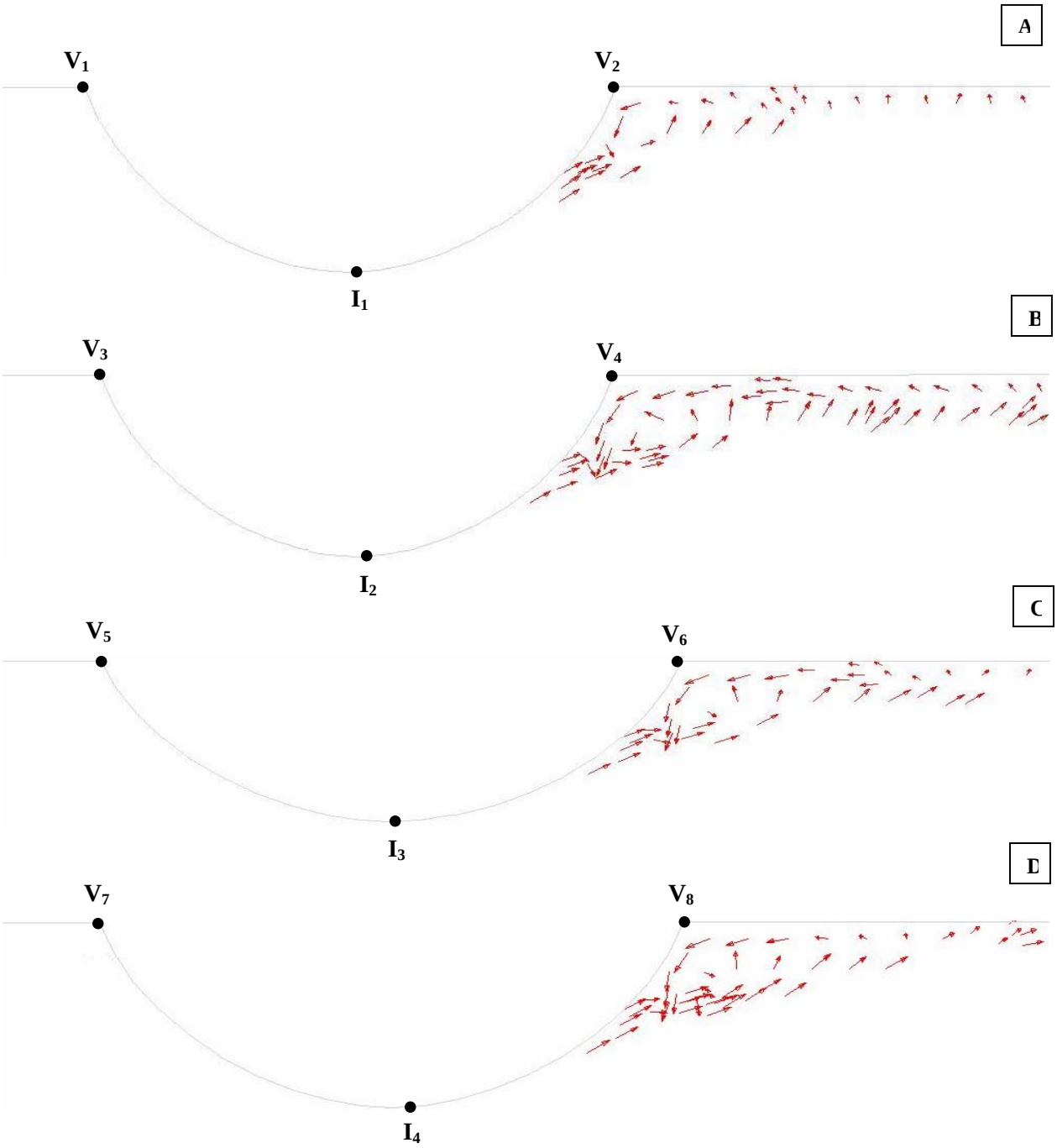

Figure 22. Vector Plot of Velocity Showing the Recirculation Zones at the Immediate Downstream of Strut Intersections 1-4 for $\tilde{Q}$ = 200 ml/min at Peak Flow (t = 2.0 s); I – Strut Intersections, V - Vertices

3.5 Recirculation Length and Height

Figure 23 shows the variation of recirculation length at the immediate downstream of each strut intersection for basal to hyperemic flow rates at times of accelerating, peak and decelerating flows. It can be seen that the flow field has complex three dimensional features during various times of the pulse cycle, particularly in the void region, causing varied recirculation lengths during accelerating, peak and decelerating flows. Maximum recirculation occurs near the entrance of the stent i.e. near the strut intersection 1. As the flow develops from strut intersection 1 to 4, the flow velocity increases and thereby the recirculation length decreases for all flow rates which aligns with the results of Barakat and Cheng [11], and Barakat and Schachter [12]. As the flow rate increases, it can be seen that the recirculation length increases. However, for hyperemic condition at peak flow (t = 2.0 s) the recirculation length is smaller near the entrance of the stent compared to that near other strut positions. This happens due to the complexity involved in the three-dimensional flow which is explained in the WSS contour plot (Fig. 21B) and velocity vector plot (Fig. 22). It can be observed that three separate recirculation zones are formed near strut cross links. At peak flow for hyperemic condition, the recirculation zones near the second strut cross-link merge together to form a single recirculation zone and hence, the recirculation length near the strut intersection 2 is higher than that near the entrance of the stent in figure 23B. The size of recirculation zones is very small at the start of pulse cycle, maximum at peak flow and decreases as the flow decelerates. For basal flow rate, maximum recirculation length of 0.13 mm occurs near the entrance of the stent which increases to 0.21 mm near the entrance for $\tilde{Q}$ = 100 ml/min, 0.3 mm near the entrance for $\tilde{Q}$ = 150 ml/min, and 0.45 mm near strut intersection 2 for hyperemic flow rate. The recirculation length increases by a factor of 3.4 from basal to hyperemic flow rates.

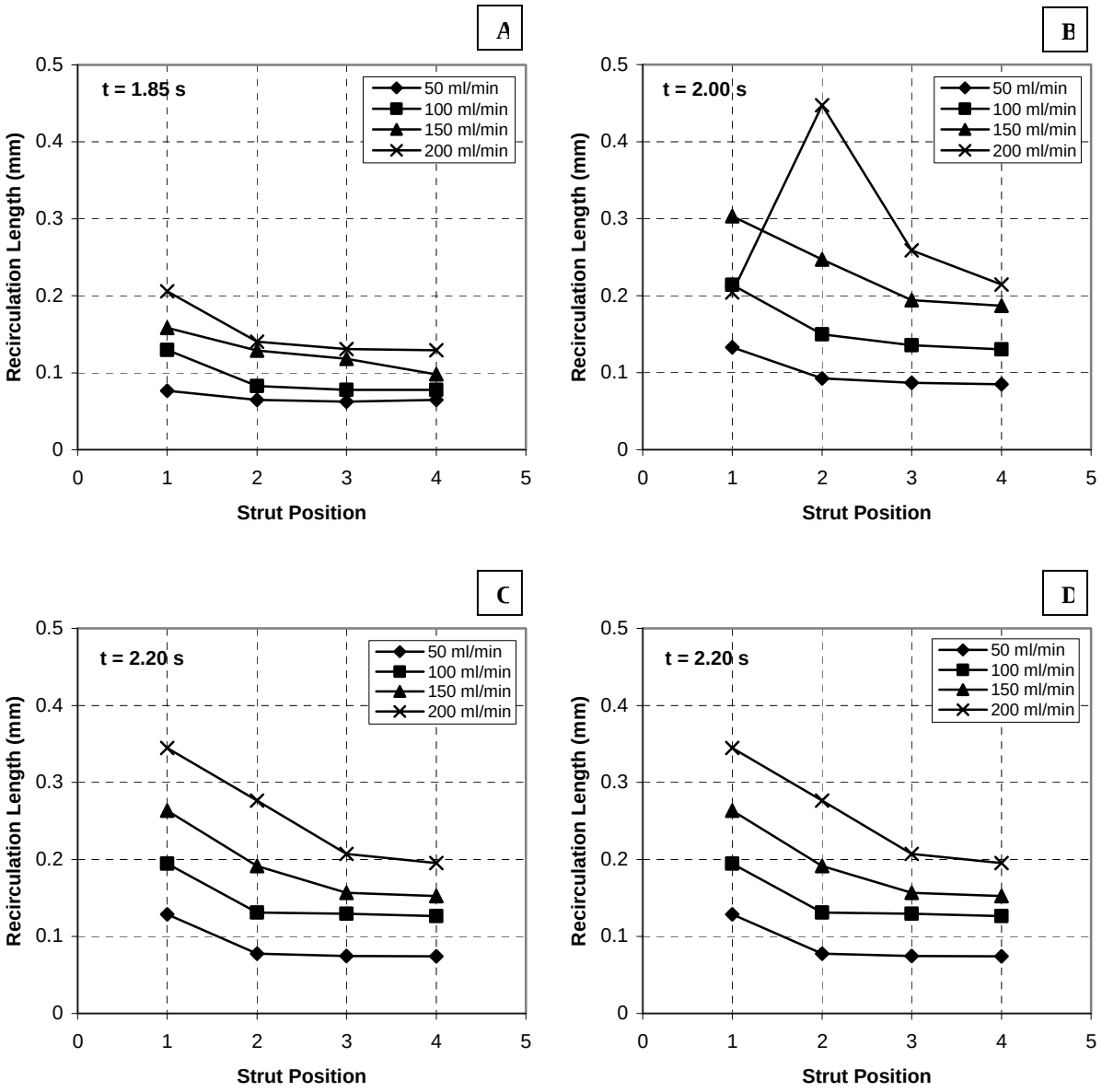

Figure 23. Variation of Recirculation Length Along the Struts

Figure 24 shows the variation of recirculation length at the immediate downstream of each strut intersection for basal to hyperemic flow rates at times of accelerating, peak and decelerating flows. Similar to the variation of recirculation length observed near the strut cross-links in figure 23, varied recirculation heights are observed in the axial flow direction which is associated with three dimensional complex fluid flow behavior. Maximum recirculation occurs near the entrance of the stent and decreases as the flow develops from strut intersections 1 to 4. For hyperemic condition at peak flow (t = 2.0 s) and at decelerating flow (t = 2.30 s), the recirculation length is smaller near the entrance of the stent compared to that near other strut positions which is similar to the variation of recirculation length. For basal flow rate, maximum recirculation height of 0.04 mm occurs near the entrance of the stent which increases to 0.058 mm near the entrance for $\tilde{Q}$ = 100 ml/min, 0.057 mm near the entrance for $\tilde{Q}$ = 150 ml/min, and 0.06 mm near strut intersection 2. The recirculation height increases by a factor of 1.5 from basal to hyperemic flow rates.

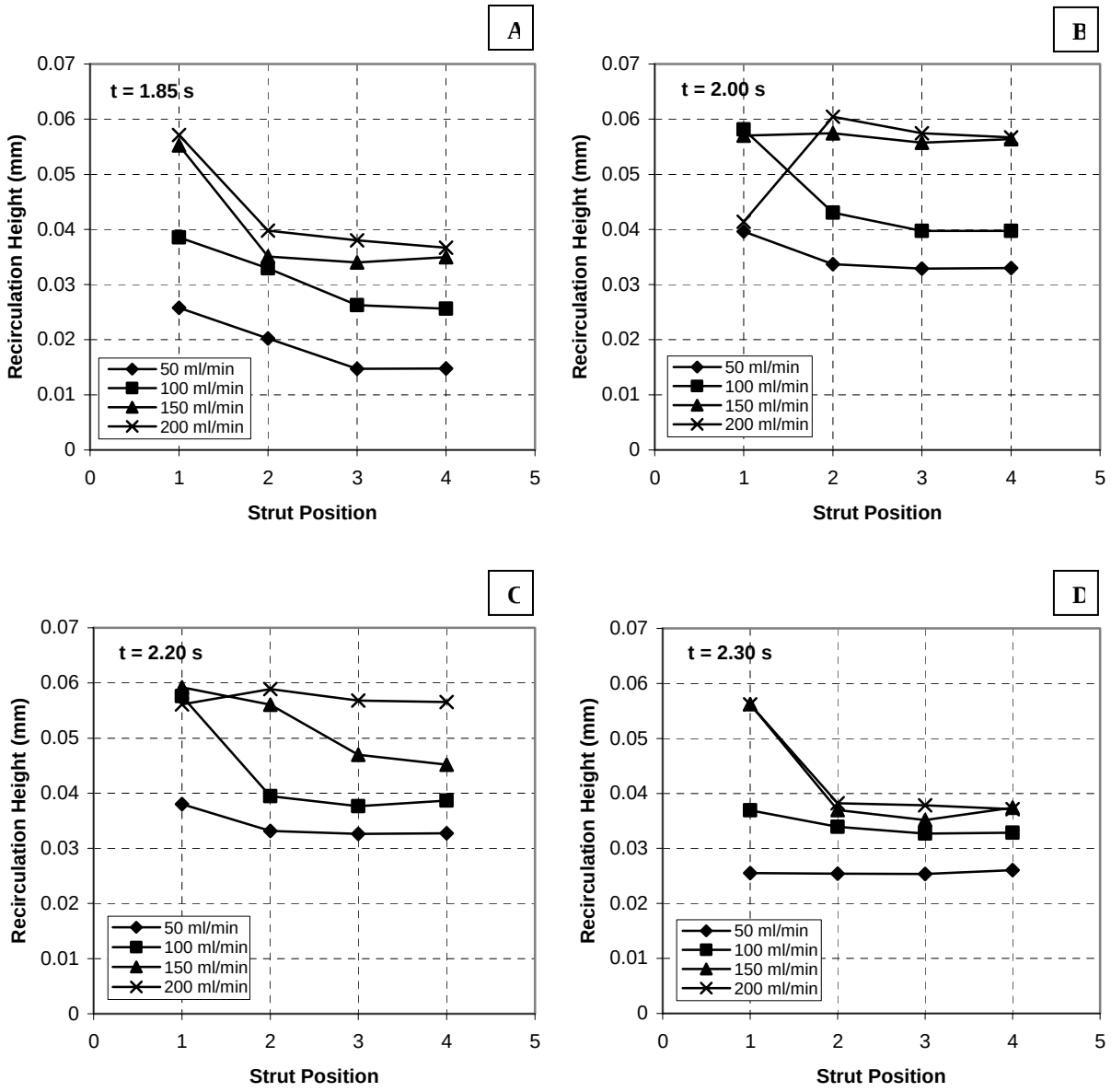

Figure 24. Variation of Recirculation Height Along the Struts

3.6 Pressure Drop

Figure 25A shows the pressure drop ($\Delta p = p_{out} - p_{in}$) between outlet and inlet of the artery for the pulse cycle. As expected, the Δp profile follows the inlet velocity profile. The existence of the stent causes the minimum pressure drop to be -0.55 mm Hg for basal flow rate and around -4 mm Hg for hyperemic flow rate at peak flow (t = 2.0 s). There is a positive Δp occurring at the end (time = 2.4 s) of the pulse cycle because of the flow reversal occurring near the arterial and stent wall regions. Integration of $\Delta p(t)$ over the pulse cycle provides the time averaged (mean) pressure drop which is shown by the horizontal lines. Each horizontal line shows the $\Delta\tilde{p}$ for each flow rate. The mean pressure drop-flow rate relation is shown in figure 25B. $\Delta\tilde{p}$ for the basal flow rate is 0.28 mm Hg and the value increases up to 1.79 mm Hg for hyperemic flow rate (a factor of 6.4 higher). Stent wall roughness values ($\Delta\tilde{p}$) were about 60% higher than (Δp_s) for the entrance region for steady flow through a smooth wall segment (diameter: 3mm and length: 10 mm) over the flow rate range as shown in Fig. 25B by the dashed curve.

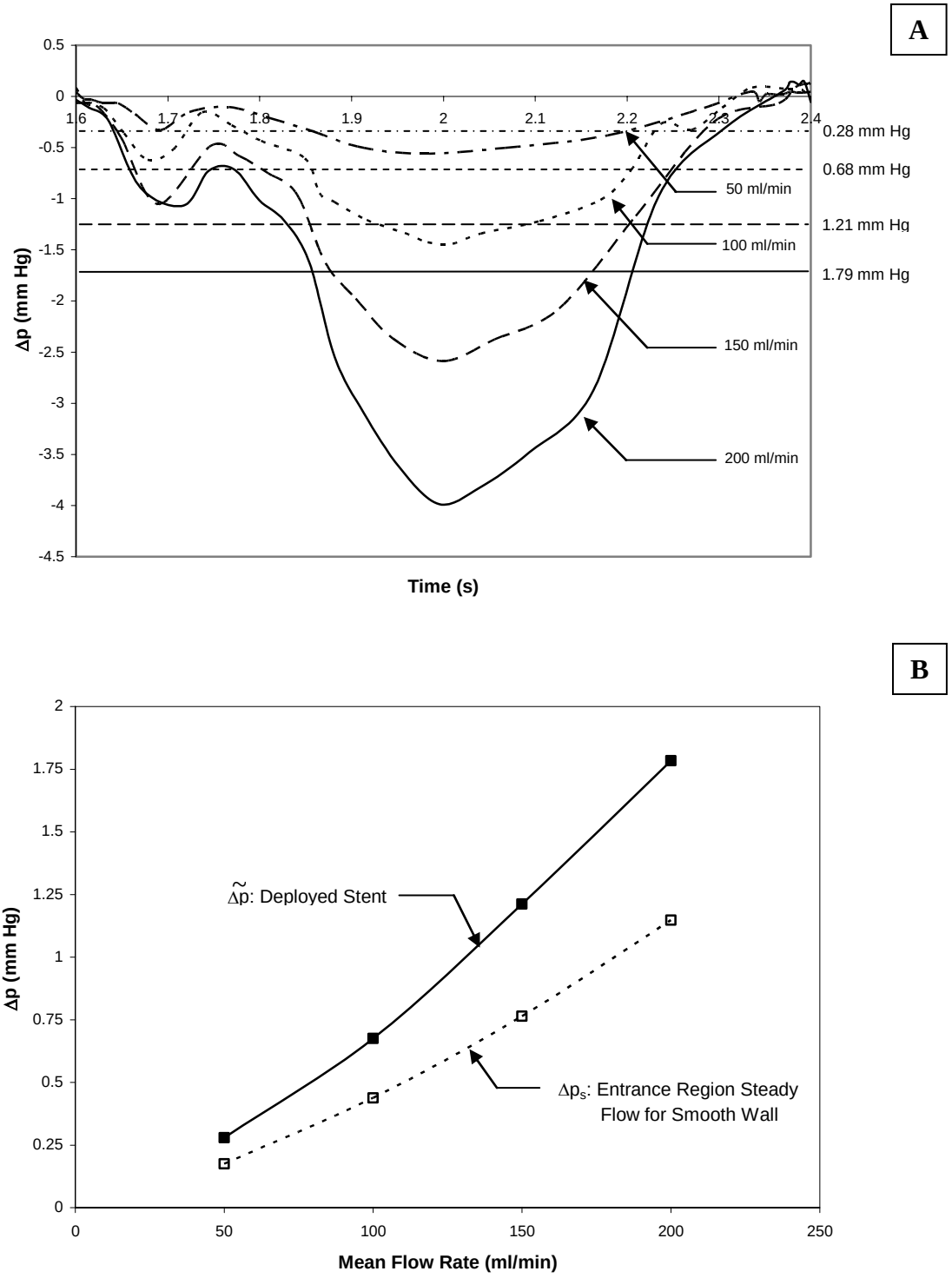

Figure 25. Pressure Drop along the Stent for a Pulse Cycle (A) and A Comparison Between a Developing Time-Averaged Mean Pressure Drop for a Deployed Stent and Steady State Developing Flow in an Unstented Coronary Artery of Same Size (B)

CHAPTER 4: DISCUSSIONS AND CONCLUSION

The current study presents a new and improved set of data for a three-dimensional hemodynamic analysis of pulsatile blood flow in a deployed coronary stent. The present investigation is different from the previous investigations as it is conducted by applying an uniform spatial inlet velocity boundary condition using a user-defined subroutine to provide a limiting condition for calculated flow parameters. Thus, the worst possible scenario of the deployed stent, i.e. the stent being placed at the entrance region of a branched coronary artery, is evaluated. The present results illustrate the changes in WSS distribution which lead to the formation of three-dimensional complex recirculation zones that may lead to restenosis. Very high values of WSS are observed over the surfaces of stent struts. Past studies report that the WSS reaching a value of 20 dyn/cm^2 over a short span depict a rapid increase in the platelets level of activation and lead to free emboli formation (Bluestein et al. [27]). The present results show very high WSS value of 530 dyn/cm^2 at the entrance of the stent for hyperemic flow rate which might have a profound impact on the arterial wall such as high level of platelet aggregation and free emboli formation. A maximum negative WSS of -200 dyn/cm^2 is observed near the entrance of the stent. WSS decreases with each subsequent strut and low WSS of 10 dyn/cm^2 is observed at the upstream of each strut intersection. Negative WSS of around -10 dyn/cm^2 is observed near the strut cross links. These portions of the vessel where there are low and negative WSS may represent locations of blood stagnation, which are susceptible to thrombus formation, platelet accumulation, smooth muscle cell proliferation and restenosis. These indicate that the immediate downstream of each strut intersection may be prone to restenosis. Maximum recirculation occurs near the entrance of the stent and the recirculation length and height decreases along the axial flow direction. Considering a complex three

dimensional flow structure within the cross-links of the struts, the left and the right side of each strut cross-link also show a persistent recirculation region. These findings have not been reported by other researchers in the past.

The limitation of the present study is that it is carried out for a straight rigid artery. However, the coronary arteries are curved and hence, there might be alterations in WSS distributions due to centrifugal force. As reported in several previous studies, diseased coronary arteries behave as rigid tubes and thus the impact of either compliant arterial wall or compliance mismatch has been ignored. To delineate the effects of compliance and compliance mismatch, further investigations are needed. Also, stent implantation resulting in residual stenosis requires investigation.

REFERENCES

[1] Heart and Stroke Statistical Update, 2001, American Heart Association, pp. 1-33.

[2] Erbel, R., Haude, M., Hopp, H.W., Franzen, D., Ruprecht, H.J., Heublin, B., Ficher, K., Jaegere, P., Serruys, P., Rutsch, W., and Probst, P., 1998, "Coronary-artery Stenting Compared with Balloon Angioplasty for Restenosis after Initial Balloon Angioplasty," Restenosis Stent Study Group, N. Engl. J. Med., **339**, pp. 1672-1678.

[3] Fischman, D.L., Leon, M.B., Baim, D.S., Schatz, R.A., Savage, M.P., Penn, I., Detre, K., Veltri, L., Ricci, D., and Nobuyoshi, M., 1994, "A Randomized Comparison of Coronary-stent Placement and Balloon Angioplasty in the Treatment of Coronary Artery Disease," Stent Restenosis Study Investigators, N. Engl. J. Med., **331**, pp. 496-501.

[4] van Beusekom, H.M., Whelan, D.M., Hofma, S.H., Krabbendam, S.C., van Hinsbergh, V.W., Verdouw, P.D., and van der Giessen, W.J., 1998, "Long-term Endothelial Dysfunction is More Pronounced after Stenting than after Balloon Angioplasty in Porcine Coronary Arteries", J. Am. Coll. Cardiol., **32**, pp. 1109-1117.

[5] Kastrati, A., Mehilli, J., Dirschinger, J., Pache, J., Ulm, K., Schuhlen, H., Seyfarth, M., Schmitt, C., Blasini, R., and Schomig, A., 2001, "Restenosis After Coronary Placement of Various Stent Types," Am. J. Cardiol., **87**, pp. 34-39.

[6] Kastrati, A., Mehilli, J., Dirschinger, J., Dotzer, F., Schuhlen, H., Neumann, F.J, Fleckenstein, M., Pfafferott, C., Seyfarth, M., and Schomig, A., 2001, "Intracoronary Stenting and Angiographic Results: Strut Thickness Effect on Restenosis Outcome (ISAR-STEREO) Trial," Circulation, **103**(23), 2816-2821.

[7] Vrints, C.J., Claeys, M.J., Bosmans, J., Conraads, V., and Snoeck, J.P., 1999, "Effect of Stenting on Coronary Flow Velocity Reserve: Comparison of Coil and Tubular Stents," Heart, **82**, pp. 465 – 470.

[8] Berry, J. L., Santamarina, A., Moore, J. E., Roychowdhury, S., and Routh, W. D., 2000, "Experimental and Computational Flow Evaluation of Coronary Stents," Ann. Biomed. Eng., **28**, pp. 386-398.

[9] Moore, J. E., and Berry, J. L., 2002, "Fluid and Solid Mechanical Implications of Vascular Stenting," Ann. Biomed. Eng., **30**, pp. 498-508.

[10] Frank, A. O., Walsh, P.W., and Moore, J. E., 2002, "Computational Fluid Dynamics and Stent Design," Artificial Organs, **26**(7), pp. 614-621.

[11] Barakat, A. I., and Cheng, E. T., 2000, "Numerical Simulation of Fluid Mechanical Disturbance Induced by Intravascular Stents," Proceedings of the 11th International Conference on Mechanics in Medicine and Biology, Maui, Hawaii, April 2-5.

[12] Barakat, A. I., and Schachter, L. G., 2001, "Computational Study of Arterial Flow Disturbance Induced by Intravascular Stents," Bioengineering Conference, BED- **50**.

[13] Caro, C. G., Fitzgerald, J. M., and Schroter, R. C., 1969, "Arterial Wall Shear and Distribution of Early Atheroma in Man," Nature, **223**, pp. 1159-1161.

[14] Nerem, R. M., and Levesque, M. J., 1987, "Fluid Mechanics in Atherosclerosis," Handbook of Bioengineering, R. Skalak and S. Chein eds., Chapter 21, 21.1-21.22.

[15] Henry, F. S., 2001, "Simulation of Flow Through Model Stented Arteries," Proceedings of the Summer Bioengineering Conference, **BED-50**, pp. 329-330.

[16] Wentzel, J.J., Krams, R., Schuurbiers, J.C.H., Oomen, J.A., Kloet, J., van der Giesen, W.J., Serruys, P.W., and Slager, C.J., 2001, "Relationship Between Neointimal Thickness

and Shear Stress After Wallstent Implantation in Human Coronary Arteries," Circulation, **103**(13), pp. 1740-1745.

[17] Wentzel, J.J., Deirdre, M.W., Van der Giesen, W.J., van Beusekom, H.M.M., Andhyiswara, I., Serruys, P.W., and Slager, C.J., Krams, R., 2000, "Coronary Stent Implantation Changes 3-D Vessel Geometry and 3-D Shear Stress Distribution," J. Biomech., **33**, pp. 1287-1295.

[18] Berry, J. L., Moore, J. E., Manoach, E., and Rolland, P. H., 2002, "Hemodynamics and Wall Mechanics of a Compliance Matching Stent: In Vitro and In Vivo Analysis," J. Vasc. Int. Rad., **13**, pp. 97-105.

[19] Fontaine, A.B., Spigos, D.G., Eaton, G., Das Passos, S., Christoforidis, G., Khabiri, H., and Jung, S., 1994, "Stent-induced Intimal Hyperplasia: Are There Fundamental Differences between Flexible and Rigid Stent Designs?," J. Vasc. Interv. Radiol., **5**, pp. 739 – 744.

[20] Rogers, C., and Edelman, E. R., 1995, "Endovascular Stent Design Dictates Experimental Restenosis and Thrombosis," Circulation, **91**, pp. 2995-3001.

[21] Edelman, E. R., and Rogers, C., 1998. "Pathobiologic Responses to Stenting," Am. J. Cardiol., **81**(7A), pp. 4E-6E.

[22] Ku, D.N., Giddens, D.P., Zarins, C.K., and Glagov, S., 1985, "Pulsatile Flow and Atherosclerosis in the Human Carotid Bifurcation. Positive Correlation between Plaque Location and Low Oscillating Shear Stress," Arterioscleosis, **5**, pp. 293 – 302.

[23] Sabbah, H.N., Khaja, F., Hawkins, E.T., Brymer, J.F., McFarland, T.M., van der Bel-Kahn, J., Doerger, P.T., and Stein, P.D., 1986, "Relation of Atherosclerosis to Arterial

Wall Shear in the Left Anterior Descending Coronary Artery of Man," Am. Heart J., **112**, pp. 453 – 458.

[24] Moore, J.E., Xu, C., Glagov, S., Zarins, C.K., and Ku, D.N., 1994, "Fluid Wall Shear Stress Measurements in a Model of the Human Abdominal Aorta: Oscillatory Behavior and Relationship to Atherosclerosis," Atherosclerosis, **110**, pp. 225 – 240.

[25] Suo, J., Oshinski, J. and Giddens, D., 2003, "Entrance Flow Patterns in the Coronary Arteries", Proceedings of the Summer Bioengineering Conference, pp. 513-514.

[26] LaDisa, J. F., Guler, I., Olson, L. E., Hettrick, D. A., Kersten, J. R., Warltier, D. C., and Pagel, P. S., 2003, "Three-Dimensional Computational Fluid Dynamics Modeling of Alterations in Coronary Wall Shear Stress Produced by Stent Implantation," Ann. Biomed. Eng., **31**, pp. 972-980.

[27] Bluestein, D., Li, Y.M., and Krukenkamp, I.B., 2002, "Free Emboli Formation in the Wake of Bi-leaflet Mechanical Heart Valves and the Effects of Implantation Techniques," J. Biomech., **35**, pp. 1553-1540.

[28] Cho, Y.I., Back, L.H., Crawford, D.W., and Cuffel, R.F., 1983, "Experimental Study of Pulsatile and Steady Flow Through a Smooth Tube and an Atherosclerotic Coronary Artery Casting of Man," J. Biomech., **16**, pp. 933-946.

[29] Sibley, D.H., Millar, H.D., Hartley, C.J., and Whitlow, P.L., 1986, "Subselective Measurement of Coronary Blood Flow Velocity Using a Steerable Doppler Catheter," J. Am. Coll. Cardiol., **8**, pp. 1332-1340.

[30] Banerjee, R. K., Back, L. H., Back, M. H., and Cho, Y. I., 2000, "Physiological flow simulation in residual human stenoses after coronary angioplasty," ASME J. Biomech. Eng., **122**(4), pp. 310-320.

[31] Banerjee, R. K., Back, L.H., and Cho, Y. I., 2000, "Computational fluid dynamics modeling techniques, using finite element methods to predict arterial blood flow," a book chapter for Biomechanical Systems Techniques & Applications: Biofluid Methods in Vascular and Pulmonary Systems, Vol. 4, Chap. 8, CRC Press.

[32] Cho, Y. I., and Kensey, K. R., 1991, "Effects of the Non-Newtonian Viscosity of Blood on Flows in a Diseased Arterial Vessel: Part I, Steady Flows," Biorheology, **28**, pp. 241-262.

[33] Fluent User Manual, ver. 6.1.18, 2003, Fluent Inc., Lebanon, NH.